

## Monitoring the Superorbital Period Variation and the Spin Period Evolution of SMC X-1

CHIN-PING HU,<sup>1,\*</sup> TATEHIRO MIHARA,<sup>2</sup> MUTSUMI SUGIZAKI,<sup>3</sup> YOSHIHIRO UEDA,<sup>1</sup> AND TERUAKI ENOTO<sup>1,4</sup>

<sup>1</sup>*Department of Astronomy, Kyoto University, Kitashirakawa-Oiwake-cho, Sakyo-ku, Kyoto 606-8502, Japan*

<sup>2</sup>*MAXI team, Institute of Physical and Chemical Research (RIKEN), 2-1, Hirosawa, Wako, Saitama 351-0198, Japan*

<sup>3</sup>*Department of Physics, Tokyo Institute of Technology, 2-12-1 Ookayama, Meguro-ku, Tokyo 152-8551, Japan*

<sup>4</sup>*The Hakubi Center for Advanced Research, Kyoto University, Kitashirakawa-Oiwake-cho, Sakyo-ku, Kyoto 606-8502, Japan*

(Accepted Sep. 27, 2019)

### ABSTRACT

The X-ray pulsar SMC X-1 shows a superorbital modulation with an unstable cycle length in the X-ray band. We present its timing behaviors, including the spin, orbital, and superorbital modulations, beyond the end of the *Rossi X-ray Timing Explorer* mission. The time-frequency maps derived by the wavelet *Z*-transform and the Hilbert-Huang transform suggest that a new superorbital period excursion event occurred in  $\sim$ MJD 57100 (2015 March). This indicates the excursion is recurrent and probably (quasi)periodic. The hardness ratio obtained with the Monitor of All-sky X-ray Image (MAXI) suggests increased absorption during the transition from the high to the low state in the superorbital cycle. Compared to the regular epochs, the superorbital profile during the excursion epochs has a shallower and narrower valley, likely caused by a flatter warp. By tracking the spin period evolution with the MAXI Gas Slit Camera in 2–20 keV, we derive an averaged spin-up rate of  $\dot{\nu} = 2.515(3) \times 10^{-11} \text{ s}^{-2}$  during the period between MJD 55141 (2009 November) and 58526 (2019 February). We obtain no positive correlation between the spin frequency residual and the superorbital frequency, but a torque change accompanying the superorbital period excursion is possible. We suggest that the accretion torque on the neutron star could be changed by various mechanisms, including the change of mass accretion rate and the warp angle. We update the value of the orbital decay as  $\dot{P}_{\text{orb}}/P_{\text{orb}} = -3.380(6) \times 10^{-6} \text{ yr}^{-1}$ . Finally, we reconfirm the detection of the superorbital modulation in the optical band and its coherence in phase with the X-ray modulation.

**Keywords:** Stars: neutron — accretion, accretion disks — X-rays: binaries — X-rays: individual (SMC X-1)

### 1. INTRODUCTION

Accreting pulsars in X-ray binaries are among the brightest and most variable X-ray emitters in the sky. The evolution of their (quasi)periodic signals, including the spin, orbital, and superorbital modulations, strongly depend on the accretion mechanisms (Corbet 1986; Corbet & Krimm 2013). Tracking their timing behaviors is helpful for understanding the connection between their accretion torque, the variability of the mass accretion rate, and the change of disk/accretion configuration. For example, the spin-up rates of OAO 1657–415 and 4U 0114+650 are different from their spin-down rates, implying the formation of a transient disk (Jenke et al. 2012; Hu et al. 2017). The superorbital modulation is

usually interpreted by the precession of the radiation-driven warped disk model (Pringle 1996; Ogilvie & Dubus 2001). The varying occultation of X-ray emission by the warped disk is thought to be the mechanism of the flux variability. The spin behavior could be associated with the change of the superorbital modulation. For instance, the pulsar in Her X-1 spins down during the anomalous low states, implying a change of disk warp angle or a change of mass accretion rate (Parmar et al. 1999; Staubert et al. 2009; Leahy & Igna 2010). Recently, it was proposed that the tidal force-induced precession of a ring on a tilted accretion disk (Inoue 2012, 2019) could be an alternative origin. The precession of such a ring tube could pass through our line of sight to the central compact object quasiperiodically and cause the superorbital modulation.

The high-mass X-ray binary (HMXB) SMC X-1 consists of a  $1.2 M_{\odot}$  neutron star and an  $18 M_{\odot}$  supergiant companion (Reynolds et al. 1993; van der Meer

Corresponding author: C.-P. Hu  
cphu@kusaastro.kyoto-u.ac.jp

\* JSPS International Research Fellow

et al. 2007; Falanga et al. 2015). Its peak luminosity reaches  $\gtrsim 5 \times 10^{38} \text{ erg s}^{-1}$ , suggesting that SMC X-1 is a mildly super-Eddington source (Price et al. 1971; Ulmer et al. 1973; Coe et al. 1981; Li & van den Heuvel 1997). The neutron star is obscured by the companion every 3.89 days (Schreier et al. 1972). From the phase evolution of the mid-eclipse time before 2000, a decay of the orbital period is observed (Levine et al. 1993; Wojdowski et al. 1998). The value of the orbital period derivative is updated as  $\dot{P}_{\text{orb}} = -3.78(15) \times 10^{-8} \text{ day day}^{-1}$  (or  $\dot{\nu}_{\text{orb}} = 2.493(1) \times 10^{-9} \text{ day}^{-2}$ , Falanga et al. 2015).

The long-term X-ray flux of SMC X-1 shows a high-low state transition with a timescale of  $\sim 60$  days (e.g., Gruber & Rothschild 1984). Later long-term observation with the all-sky monitor (ASM) on board the *Ross X-ray Timing Explorer (RXTE)* suggests that the cycle length of this superorbital modulation is unstable (Wojdowski et al. 1998; Clarkson et al. 2003). The time-frequency map obtained from the ASM light curve shows two excursion events in  $\sim \text{MJD } 50800$  and  $\sim \text{MJD } 54000$ , where the superorbital period evolves to  $P_{\text{sup}} \sim 40$  days (Trowbridge et al. 2007; Hu et al. 2011). Except for these two events, the superorbital period is relatively stable at  $P_{\text{sup}} \sim 56$  days, though short-term variabilities remain possible.

The compact object in SMC X-1 is an X-ray pulsar with a spin period of 0.7 s (Lucke et al. 1976). The pulse profile varies with the energy bands, orbital phase, and superorbital phase. The hard X-ray pulse profile is relatively stable and superorbital phase-independent, suggesting that it is originated from the pencil beam from the polar cap (Neilsen et al. 2004). On the other hand, the soft X-ray profile is highly variable with superorbital phase (Wojdowski et al. 1998; Neilsen et al. 2004). It is interpreted as the reprocessing of X-rays from the accretion disk (Hickox & Vrtilek 2005). Since 1997, SMC X-1 has been well monitored with several X-ray instruments, and the most frequent monitoring was carried out with *RXTE* between 1996 and 2000 (Henry & Schreier 1977; İnam et al. 2010). The full history of the pulse frequency evolution of SMC X-1 up to MJD 52987 (2003 December 14) is reported by İnam et al. (2010). The frequency almost increases with time monotonically, but the spin-up rate changes significantly. The spin history can be divided into five epochs with a frequency derivative varying in the range of  $(2 - 3.6) \times 10^{-11} \text{ s}^{-2}$ . The spin-up rate could be associated with the drift of the superorbital modulation period (Dage et al. 2019). Their correlation remains inconclusive through a detailed analysis, but the superorbital period excursion on  $\sim \text{MJD } 50800$  coincides with a change in the spin-up rate.

The major goal of this research is to explore the connection between the spin, orbital, and superorbital modulations. With the ongoing observation made with the *Neil Gehrels Swift Observatory* (hereafter *Swift*) and the Monitor of All-sky X-ray Image (MAXI), we extend  $\sim 7$

yr of the time baseline after the *RXTE* era. We would like to confirm whether the superorbital period excursion is recurrent and examine whether the short-term period drifting is real. We also process the new *Chandra*, *XMM-Newton*, and *Swift* X-Ray Telescope (XRT) observations, as well as the photon events collected with MAXI, to extend the history of the pulse frequency measurements. This is used to examine whether there is any connection between the spin and the superorbital modulations. Moreover, we revisit the superorbital dependence of the orbital profile using MAXI data to see if the orbital profile in different superorbital phases is energy-dependent. Section 2 introduces the observation and data reduction. Then, we present the analysis result for the superorbital period excursion, orbital ephemeris and profile, and spin period evolution in Section 3. We also analyze the optical data taken with the All-Sky Automated Survey for Supernovae (ASAS-SN; Shappee et al. 2014; Kochanek et al. 2017) to examine the orbital and superorbital modulation in the optical band. We discuss the implications of our discoveries in Section 4 and summarize our work in Section 5.

## 2. OBSERVATIONS AND DATA REDUCTION

### 2.1. X-ray Monitoring Data

We investigate the superorbital modulation using the data taken with the ASM on board *RXTE*, the Burst Alert Telescope (BAT) on board *Swift*, and the Gas Slit Camera (GSC) on board MAXI. We use the dwell data of ASM and one-satellite-orbit binned light curve of *Swift* BAT and MAXI to investigate the orbital modulation. The exposure time of the ASM dwell light curve, the time resolution of the one-satellite-orbit binned BAT and MAXI light curves, and the time coverage and the energy range of these three satellites are summarized in Table 1. We rebin the light curves with a resolution of 1 day to trace the superorbital modulation of SMC X-1. We further utilize the photon events collected with the MAXI GSC to track the spin period evolution of SMC X-1.

The ASM consists of three proportional counterarrays with a collecting area of  $90 \text{ cm}^2$  (Levine et al. 1996). The energy range of the ASM is 1.5–12 keV and can be divided into three bands, 1.5–3, 3–5, and 5–12 keV to provide X-ray hardness information. It swept the entire sky every  $\sim 90$  minutes from 1996 to 2012. We exclude the data collected after MJD 55400 (2010 July) because the gain of the ASM changes significantly and the superorbital modulation is difficult to recognize (Levine et al. 2011). To eliminate possible contamination from the bad data points or extremely short exposures, we filter these data points with uncertainties that are  $3\sigma$  higher than the mean uncertainty. We also remove data points with background count rates that are  $3\sigma$  higher than the mean level.

The BAT onboard *Swift* is designed to trigger alerts of gamma-ray bursts. It has a large collecting area

**Table 1.** Data Sets Used in This Work.

Instrument	ObsID	MJD Range	Energy (Wavelength)	Time Resolution
X-Ray All-Sky Monitoring Programs				
<i>RXTE</i> ASM	...	50123–55200	1.5–12 keV	90 minutes
<i>Swift</i> BAT	...	53416–58565	15–50 keV	96 minutes
MAXI GSC	...	55058–58565	2–20 keV	92 minutes
MAXI GSC (events)	...	55058–58565	2–20 keV	50 $\mu$ s
Pointed X-Ray Observations				
<i>Chandra</i> HRC	14054	55969.37–55970.26	0.08–10 keV	16 $\mu$ s
<i>XMM-Newton</i> PN	0784570201	57639.93–57640.14	0.3–10 keV	30 $\mu$ s
<i>XMM-Newton</i> PN	0784570301	57650.32–57650.54	0.3–10 keV	30 $\mu$ s
<i>XMM-Newton</i> PN	0784570501	57685.91–57686.13	0.3–10 keV	30 $\mu$ s
<i>Swift</i> XRT	00081950001	57650.15–57650.55	0.3–10 keV	1.8 ms
<i>Swift</i> XRT	00081950002	57685.21–57685.94	0.3–10 keV	1.8 ms
Optical Survey				
ASAS-SN (V-band)	...	56792–58385	551(83) nm <sup>a</sup>	90 s
ASAS-SN (g'-band)	...	58002–58483	480(141) nm <sup>a</sup>	90 s

<sup>a</sup>This value denotes the central wavelength of the filter. The FWHM of the filter is shown in the parentheses.

(5200 cm<sup>2</sup>) and has monitored known X-ray sources in the hard X-ray (15–150 keV) since 2004 (Barthelmy et al. 2005). The entire sky can be scanned once every  $\sim$ 96 minutes. We use the 15–50 keV light curve provided by the hard X-ray transient monitor program (Krimm et al. 2013). We apply the same selection criterion on the uncertainties as for the ASM data to filter the light curve.

MAXI is a payload mounted on the Japanese Experimental Module of the *International Space Station* (*ISS*). Similar to the ASM, it can monitor the entire sky in the X-ray band (Matsuoka et al. 2009). MAXI is equipped with two cameras: the solid-state slit camera (SSC) with a collecting area of 200 cm<sup>2</sup> in the energy range of 0.5–12 keV, and the GSC, with a collecting area of 5350 cm<sup>2</sup> in the energy range of 2–30 keV. We investigate the orbital and superorbital modulations of SMC X-1 with the GSC light curve provided by RIKEN, JAXA, and the MAXI team. The energy range of the archival binned light curves is 2–20 keV. The hardness information can also be obtained because the light curves are further divided into 2–4, 4–10, and 10–20 keV bands. We apply the same selection criterion on the uncertainties as for the ASM data to filter the light curve.

Except for the archival light curves, we search for pulsation signal and track the spin period evolution of SMC X-1 using photon events collected with MAXI. We only use photons collected with the GSC owing to its excellent time resolution of 50  $\mu$ s (20 kHz clock counter; Mihara et al. 2011), which is suitable to track the evo-

lution of accreting pulsars (see, e.g., Takagi et al. 2016; Yatabe et al. 2018). The data transmission from the *ISS* to the ground has three reduction modes: 64, 32, and 16 bit, due to the limited telemetry bandwidth. We use 64 bit data because they contain precise timing information (Mihara et al. 2011). The GSC consists of 12 proportional counters (GSC ID 0, 1, ..., 9, A, B) encapsulated in two mission data processors (Mihara et al. 2011); GSC 3, 6, and 9 are out of order, and GSC A, B stopped working before 2010 (see Section 2.3 in Sugizaki et al. 2011). Therefore, we only use data with GSC IDs of 0, 1, 2, 4, 5, 7, and 8. We extract X-ray photons in 2–20 keV before MJD 58565 using `mextract` from the MAXI database and correct the arrival time of each photon to the barycenter of the solar system. We extract the source photons from a 1 $^\circ$  radius circle centered on SMC X-1. Nearly 90% of the source photons are encircled (Mihara et al. 2011).

## 2.2. Pointed X-Ray Observations

The pointed observations made with *Chandra*, *XMM-Newton*, and *Swift* XRT are ideal benchmarks for tracking the spin period evolution and searching for the spin period with MAXI GSC events (see Section 3.2). The basic information of pointed observations used in this work is summarized in Table 1.

Between 2001 and 2016, SMC X-1 was observed with *Chandra* 19 times. The spin period measurements in 2001–2002 are reported in Neilsen et al. (2004). The observation in 2013 (ObsID 14054) was made with the

High Resolution Camera (HRC) with a time resolution of 10 ms, enough to resolve the spin signal of SMC X-1. Ten other observations during 2012 and 2016 were made with the high-energy transmission grating in timed-exposure mode. We do not make use of these data due to their insufficient time resolution. We reprocess the data (ObsID 14054) using the pipeline `chandra_repro` in the *Chandra* Interactive Analysis of Observations (CIAO) version 4.9 with the calibration database (CALDB) version 4.7.3 (Fruscione et al. 2006). We correct the arrival time of each photon to the barycenter of the solar system using the `axbary` tool. We extract the source events from a circular aperture of  $2''$  radius.

Seven observations are carried out by *XMM-Newton* where SMC X-1 is in the field of view. The spin period obtained from two 2001 observations (ObsIDs 0011450101 and 0011450201) are reported in Neilsen et al. (2004). The main target of the observation made in 2006 (ObsID 0311590601) is Nova SMC 2005, and SMC X-1 is in the field of view. However, this observation was made during the eclipse; hence, we could not search for pulsation. In 2016, *XMM-Newton* carried four observations (ObsIDs 0784570201, 0784570301, 0784570401, and 0784570501). The PN detector is operated in timing mode, which is ideal for our purpose owing to its excellent time resolution of  $30 \mu\text{s}$ . We perform basic data reduction with the task `epproc` of the *XMM-Newton* Science Analysis System (SAS). We filter out the time intervals with strong background flaring and correct the photon arrival time to the barycenter using the `barycen` task. The source events are extracted from 19 pixels in RAWX around the source. This corresponds to a  $1'.3 \times 13'.5$  box on the sky. We exclude the dataset with ObsID 0784570401 in the following analysis, because it is made during the superorbital low state and the spin signal cannot be detected.

Twice in 2016, SMC X-1 was observed with *Swift* where the XRT was operated in the windowed timing mode that provides a high time resolution of 1.8 ms. We utilize the task `xrtpipeline` to create cleaned level 2 event files. The image is compressed into one dimension. We choose the source events from a  $60''$  wide box from SMC X-1 to ensure that  $\sim 90\%$  of photons are collected. The vertical size corresponds to  $8'$  on the sky. The barycentric correction is achieved using the tool `barycorr`.

### 2.3. Optical Light Curve

We retrieve the optical light curve of SMC X-1 from the ASAS-SN sky patrol<sup>1</sup> to independently confirm the orbital and superorbital modulations obtained by the Optical Gravitational Lensing Experiment (OGLE) in the *I* band (Coe et al. 2013). The ASAS-SN has scanned the entire sky every 2–3 days in the *V* band since 2013

and the *g* band since 2017. SMC X-1 is monitored since May 2014. Roughly  $\sim 1300$  exposures in *V*-band and  $\sim 900$  exposures in *g*-band are used in this research. The exposure time of each snapshot is 90 s. The limiting magnitude of each exposure varies between observations but is concentrated in  $V = 15.3 - 16.3$  and  $g = 15.5 - 16.5$ , which is two magnitude fainter than the typical apparent magnitude of SMC X-1 ( $V \sim 13.15$  and  $g \sim 13.05$ ). We remove those data points without magnitude measurement and filter out those data points with uncertainties that are  $3\sigma$  higher than the mean uncertainty. The observational periods of the *V* and *g* bands have a 1 yr overlap between MJD 58002 and 58385. The MJD range of the ASAS-SN data used in this analysis is described in Table 1.

## 3. ANALYSIS AND RESULT

In this section, we describe the analysis technique and the result of the superorbital, orbital, and spin period evolution. The result of the superorbital modulation is described in Section 3.1. We first utilize two time-frequency analysis methods to track the evolution of the superorbital modulation frequency and find a new excursion event (Section 3.1.2). Then we study the superorbital profile in detail, including the hardness ratio (HR) variability, the connection between the modulation amplitude and cycle length, and the high-/low-state flux variability (Section 3.1.3 and 3.1.4). In Section 3.2, we track the spin frequency evolution of SMC X-1 with both pointed X-ray observations and the MAXI GSC event files. We deeply investigate the connection between the spin frequency residual and the superorbital frequency. By tracking the phase shift of the mean longitude of the orbit, we refine the orbital ephemeris (Section 3.2.2). In Section 3.3, we investigate the detailed orbital profile and the HR in different superorbital states with the MAXI GSC. Finally, we study the orbital and superorbital modulations in the optical band in Section 3.4.

### 3.1. Superorbital Modulation

The variability of the superorbital period before  $\sim$ MJD 55500 has been carried out with the *RXTE* ASM data (Hu et al. 2011; Dage et al. 2019). We analyze the data collected with the *Swift* BAT and MAXI GSC to extend the time baseline to 2019 March ( $\sim$ MJD 58560) and track the superorbital evolution of SMC X-1 beyond the *RXTE* era. We use the weighted wavelet *Z*-transform (WWZ; Foster 1996) and the Hilbert-Huang transform (HHT; Huang et al. 1998) to analyze the data.

#### 3.1.1. Time-frequency Analysis Algorithms

The WWZ is based on the Morlet wavelet algorithm and generalized to unevenly sampled time series. The wavelet function is a sinusoidal wave convolved by a Gaussian envelope (Grossmann & Morlet 1984). The

<sup>1</sup> <https://asas-sn.osu.edu/>



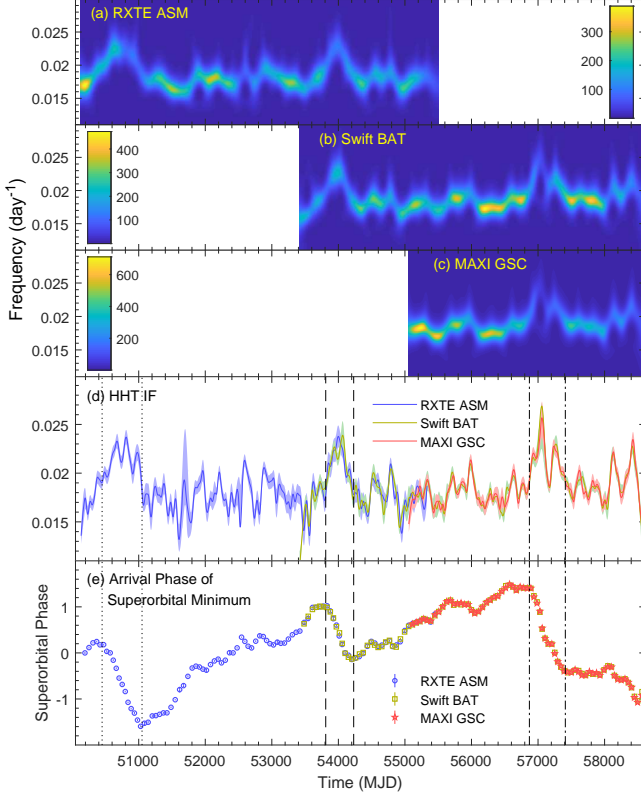


**Figure 1.** The WWZ spectra of SMC X-1 obtained from (a) *RXTE* ASM, (b) *Swift* BAT, and (c) MAXI GSC light curves. The color bar denotes the  $Z$  value of WWZ spectra. The instantaneous frequencies obtained from the *RXTE* ASM (blue), *Swift* BAT (green), and MAXI GSC (red) light curves with the HHT are plotted in panel (d). The frequencies are smoothed, and the corresponding shaded areas denote 95% confidence intervals. The arrival phase of the minimum of the superorbital modulation is shown in panel (e). Three excursion epochs (see Table 2 for definition) are labeled as dotted, dashed, and dashed-dotted vertical lines.

wavelet of a trial frequency  $\omega$  at a time  $\tau$  is

$$F(t) = e^{i\omega(t-\tau) - c\omega^2(t-\tau)^2}, \quad (1)$$

where  $c$  is a constant to scale the width of the Gaussian envelope.

The HHT contains two steps: (i) decompose the light curve into intrinsic mode functions (IMFs) with empirical mode decomposition (EMD) and (ii) perform the Hilbert transform or other algorithms, e.g., direct quadrature or generalized zero-crossing, to yield the instantaneous frequency. The instantaneous frequency can be calculated from any time series, but it is physically meaningful only if the time series is an IMF. Two criteria should be satisfied for an IMF: (i) the number of extrema and the number of zero crossings must be identical or, at most, differ by one; and (ii) the local mean

value defined by the average of the upper and lower envelopes must be zero (Huang et al. 1998). They are nearly impossible for the real data, and hence the EMD is proposed (Huang et al. 1998). A time series  $x(t)$  can be expressed as

$$x(t) = \sum_{j=1}^n c_j(t) = \sum_{j=1}^n a_j(t) e^{i \int \omega_j(t) dt}, \quad (2)$$

where  $c_j(t)$  is the decomposed IMFs,  $a_j(t)$  is the instantaneous amplitude,  $\omega_j(t)$  is the instantaneous frequency of the  $j$ th IMF, and  $n$  is the number of IMFs. In general,  $n \leq \log_2 N$  where  $N$  is the number of total data points in  $x(t)$ . Compared to the Fourier analysis, the HHT decomposes the time series into fewer components, but the amplitude and frequency of each component are functions of time.

However, a signal with a consistent modulation timescale could be decomposed into different IMFs using EMD. This “mode-mixing” problem is solved by the assistance of white noise (EEMD; Wu & Huang 2009). For each trial, a white-noise series with a finite amplitude is added to the data. We then obtain the mean of each IMF by

$$c_j = \frac{1}{M} \sum_{k=1}^M c_{jk} \quad (3)$$

where  $M$  is the number of total trials. A remaining problem is that the summation of IMFs is no longer an IMF. We apply a post-processing EMD to deal with this problem (see Wu & Huang 2009, for a detailed procedure). This algorithm has been successfully used to analyze the *RXTE* ASM light curve of SMC X-1 (Hu et al. 2011).

Recently, the EEMD has been further improved by adding a pair of positive and negative white noises to optimize the completeness of the IMFs (Yeh et al. 2010). This is included in the Matlab fast EEMD package developed by the Research Center for Adaptive Data Analysis at National Central University (Wang et al. 2014)<sup>2</sup>. This computationally efficient algorithm allows us to perform a Monte Carlo simulation and estimate the confidence interval of the instantaneous frequency obtained with the normalized Hilbert transform. We generate  $10^4$  simulated light curves based on the observed count rate plus a Gaussian-distributed noise with the standard deviation equal to the uncertainty. For each light curve, we obtain the instantaneous superorbital frequency. We then take the average of the instantaneous frequency at day.

### 3.1.2. Superorbital Period Excursions

<sup>2</sup> <http://in.ncu.edu.tw/ncu34951/research1.htm>

**Table 2.** Averaged Superorbital Modulation Period of SMC X-1 in Five Epochs.

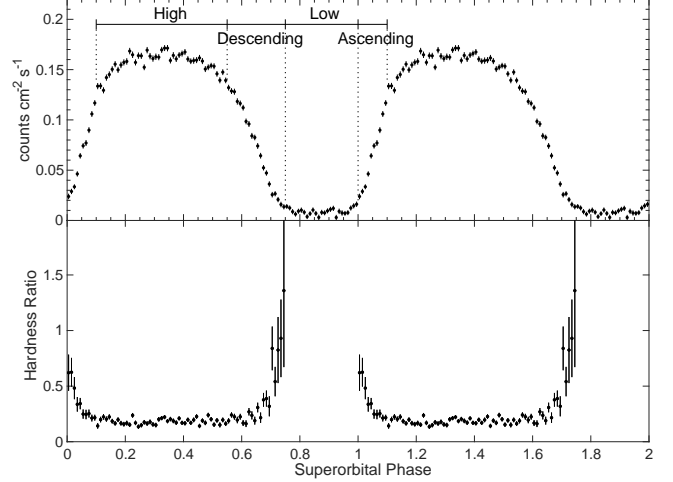
MJD Range	Epochs	Mean Period (days)
50450–51050	Excursion	45.8(2)
51050–53810	Regular	56.9(1)
53810–54230	Excursion	45.8(3)
54230–56870	Regular	56.1(1)
56870–57410	Excursion	45.2(3)

NOTE—The uncertainties are  $1\sigma$  statistical uncertainties, which may be underestimated because the period has short-timescale variability.

The resulting WWZ spectra of the *RXTE* ASM, *Swift* BAT, and MAXI GSC light curves are plotted in Figure 1 (a)–(c), while the mean instantaneous frequencies obtained with the HHT are plotted in Figure 1(d). The mean instantaneous frequencies are smoothed by a local regression smoothing weighted by a tricube function to emphasize the structures longer than one superorbital cycle (Cleveland 1979; Cleveland & Devlin 1988). The 95% confidence intervals obtained from all three observatories are plotted in Figure 1(d).

From the WWZ and the HHT results, we observe that the superorbital frequency evolved to  $f_{\text{sup}} \approx 0.025$  ( $P_{\text{sup}} \approx 40$  days) around  $\sim$ MJD 57100, similar to the previous two excursion events on  $\sim$ MJD 50800 and  $\sim$ MJD 54000. The latter two events on  $\sim$ MJD 54000 and  $\sim$ MJD 57100 are independently observed by at least two satellites. The time interval between two successful excursion events is  $\sim 3150$  days, implying that the excursion event is recurrent and possibly periodic.

The EEMD is equivalent to a local dyadic filter and can be used to filter high-frequency noise. For each dataset, we combine the IMFs from the  $c_5$  (dominated by the superorbital modulation; see Hu et al. 2011) to the residual to obtain a high-pass-filtered light curve, similar to the operation to the quasiperiodic oscillation in RE J1034+396 (Hu et al. 2014). We then get the arrival time of each superorbital minimum. The uncertainty of the arrival time of each superorbital minimum is estimated by the Monte Carlo simulation. We plot the evolution of the arrival phase with a 54.3 day folding period in Figure 1(e). The arrival times of superorbital minima determined with the *RXTE* ASM, *Swift* BAT, and MAXI GSC are listed in Table 6 of Appendix A. We identify three major excursion epochs and two regular epochs from the phase evolution. We define the excursion epoch as the period when the arrival phase of the superorbital minimum decreases more than one cycle. Two regular epochs are then defined as the intervals between these three excursion epochs. The

**Figure 2.** (Top) MAXI GSC 2–20 keV light curve folded with the superorbital phase defined with the HHT. (Bottom) HR vs. superorbital phase. The bin size is 1/100 cycle, where HR values in superorbital phase  $0.75 \leq \phi_{\text{sup}} < 1.0$  are not presented.

mean superorbital periods in these five epochs are listed in Table 2. The mean superorbital periods during the major excursion epochs are as short as  $\sim 45$  days. In contrast, the mean superorbital period is  $\sim 56$  days in the regular epochs. The phase evolution of these two regular epochs is not stable, but the patterns are similar. A humpy pattern can be seen during the middle  $\sim 1000$  days of the regular epoch, and a few minor excursions that contain to to five superorbital cycles with  $P_{\text{sup}} \lesssim 50$  days occasionally occur. The phase of the last few cycles after  $\sim$ MJD 58000 drops significantly. This coincides with the variation toward shorter superorbital periods (see Figure 1(a)–(d)). In the current stage, we could not conclude whether it indicates a new major period excursion event or a minor excursion event similar to those near  $\sim$ MJD 52000, and  $\sim$ MJD 56000.

### 3.1.3. Superorbital Profile

The superorbital profile can be obtained according to the instantaneous phase derived in the HHT. The profile shapes obtained from the *RXTE* ASM, *Swift* BAT, and MAXI GSC are fully consistent with each other, implying that the mechanism is nearly energy-independent. The superorbital profile observed with the MAXI GSC is shown in Figure 2. We assign the start of the ascending as phase zero. The profile shows an ascending lasting  $\sim 0.1$  cycles (from phase 0–0.1), a high state at phase 0.1–0.55, a descending at phase 0.55–0.75, and a low state at phase 0.75–1.0.

The spectral variability can be obtained with the variability of the HR. Utilizing the *RXTE* ASM data, it has been suggested that the emission during the low state is dominated by hard X-rays (Trowbridge et al. 2007). In this research, we investigate the detailed HR variability

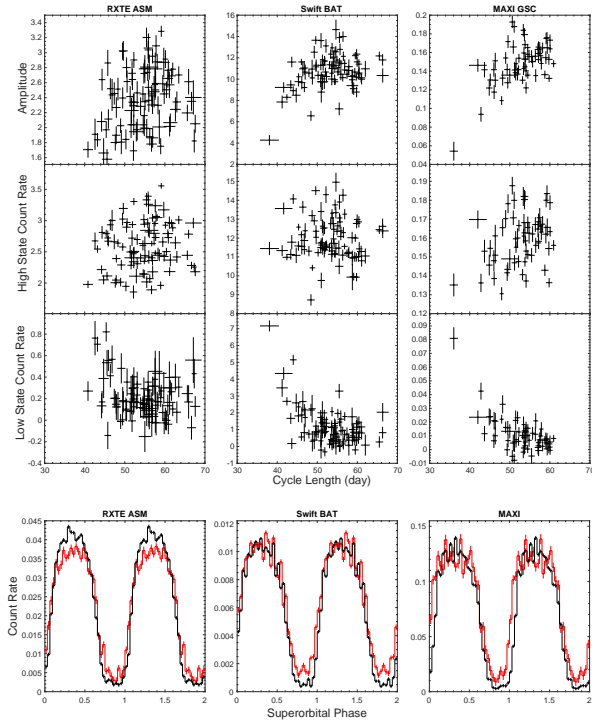


**Figure 3.** (Top) Modulation amplitude, the high-state count rate, and the low-state count rate versus the superorbital cycle length. (Bottom) Superorbital profiles in excursion epochs (red) and regular epochs (black).

with the MAXI GSC. The HR is defined as

$$\text{HR} = \frac{\text{ch2} - \text{ch1}}{\text{ch2} + \text{ch1}}, \quad (4)$$

where ch1 is the count rate in 2–4 keV, and ch2 is the count rate in 4–10 keV. A high HR value implies that the emission is dominated by hard X-rays. We first create a superorbital profile in each band by dividing a superorbital cycle into 100 bins. Then we calculate the HR value in each bin using Equation 4. The X-ray photons collected during the eclipse are excluded. The superorbital and the HR profiles are shown in Figure 2. We find that the HR values fluctuate significantly and have extremely large uncertainties in the superorbital phase  $0.75 \leq \phi_{\text{sup}} < 1.0$ . We remove the corresponding data points because SMC X-1 is unlikely to be detectable during the superorbital low state. The HR is stable at  $\sim 0.25$  during the high state, while it gradually decreases in the ascending state and gradually increases in the descending state. This is the first time we witness the change of HR in the transition with X-ray monitoring data. This suggests a possible variability of X-ray absorption caused by a gradual change of the optical depth (Inam et al. 2010).

### 3.1.4. Correlation between Superorbital Amplitude and Cycle Length

It is suggested that the superorbital modulation amplitude may marginally correlate with the superorbital cycle length (Hu et al. 2011). We reexamine this correlation with new *Swift* BAT and MAXI GSC datasets. The cycle length is obtained from the HHT phase, where the uncertainty can be estimated by the Monte Carlo simulation in Section 3.1.2. We also try to define the cycle length from the time interval between two neighboring superorbital minima or maxima, and the result is fully consistent. In each cycle, we obtain an amplitude from the difference between the averaged high-state count rate and the averaged low-state count rate. This is a more detailed analysis than the rms amplitude presented in Hu et al. (2011) because the variability of high- and low-state fluxes could be originated from different mechanisms.

The top panel of Figure 3 shows the superorbital amplitude and high-/low-state count rates versus superorbital cycle length. We find that the correlation between modulation amplitude and the cycle length is not well determined in *RXTE* ASM data but can be seen in the *Swift* BAT and MAXI GSC data. The Pearson’s linear correlation coefficient of *Swift* BAT result is  $r = 0.34$ , with a null hypothesis probability of  $p = 9.1 \times 10^{-4}$ . The correlation obtained from the MAXI GSC is  $r = 0.57$ , with a null hypothesis probability of  $p = 8.4 \times 10^{-7}$ . We examine the high- and low-state count rates and find that the correlation is dominated by the variability of the count rate in the low state. The correlation coefficient between the cycle length and the low-state count rate in the BAT data set is  $r = -0.52$  with  $p = 6.5 \times 10^{-8}$ , while it is  $r = -0.64$  with  $p = 1.5 \times 10^{-6}$  for the MAXI GSC. The Pearson’s correlation assumes a linear relationship that may not be suitable for our dataset. Therefore, we use the nonparametric Kendall’s correlation coefficient ( $\tau_k$ ) to further test the correlation between the cycle length and the low-state count rate. For the BAT data set, we obtain  $\tau_k = -0.27$  with  $p = 1.7 \times 10^{-4}$ , while for the MAXI data, we obtain  $\tau_k = 0.35$  with  $p = 7.4 \times 10^{-5}$ . Considering that the correlation does not take the uncertainties into account, we perform  $10^6$  times Monte Carlo simulations. In each trial, we generate a fake dataset of cycle length and amplitude. For each data point, we assign the values by generating two Gaussian-distributed random numbers centered on the observed values of cycle length and amplitude and  $\sigma$  equal to the uncertainties. The resulting distribution of the correlation coefficient is well concentrated near the observed value with a limited deviation. The mean value of  $\tau_k$  between the cycle length and the low-state count rate in the *Swift* BAT dataset is  $-0.27$  with a standard deviation of 0.03, while the mean and standard deviation values for the MAXI data set are  $-0.34$  and 0.04, respectively.

However, the correlation could be dominated by a few outliers. We use the bootstrap resampling technique with  $10^7$  simulations to test whether the observed cor-

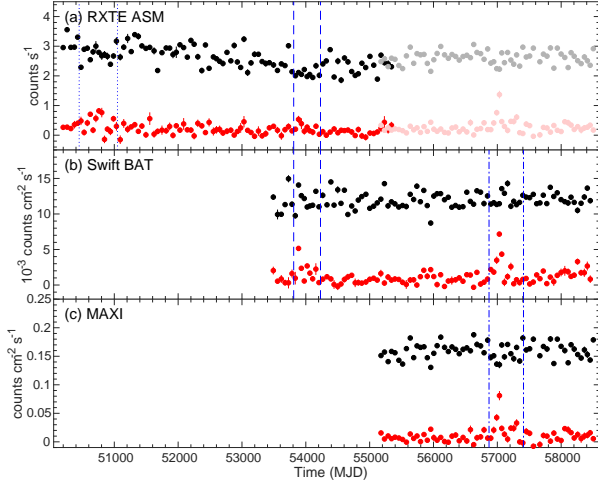


**Figure 4.** Mean count rates for the superorbital high state (black) and low state (red) observed with the *RXTE* ASM, *Swift* BAT, and MAXI GSC. The MAXI count rate is converted to the *RXTE* ASM count rate and stacked in panel (a) with corresponding light colors. The first, second, and third superorbital excursion epochs are denoted by dotted, dashed, and dashed-dotted vertical blue lines, respectively.

relation is biased (Efron 1979). The mean value of  $\tau_k$  between the cycle length and the low-state count rate of the *Swift* BAT data is  $-0.28 \pm 0.07$ , where the probability that showing a positive correlation is  $3.5 \times 10^{-4}$ . The mean value of  $\tau_k$  of the MAXI GSC data is  $-0.36 \pm 0.08$  with a probability of  $7.3 \times 10^{-5}$  that showing  $\tau_k > 0$ . This result indicates that the negative correlation is not accidental. In contrast, the ASM data set has a mean correlation coefficient of  $-0.11$  with a standard deviation of  $0.07$ , and roughly 8% of the resampled sets result in a positive correlation, indicating a marginal anticorrelation.

The true correlation between the cycle length and the low-state count rate may not be linear, although the linear correlation coefficient is significant. From the *Swift* BAT and MAXI observations, we note that the low-state count rate is nearly a constant for  $P_{\text{sup}} \gtrsim 50$  days. Therefore, the correlation could be dominated by the low-state count rate with  $P_{\text{sup}} \lesssim 50$  days, corresponding to the superorbital excursion events. Similar behavior can also be seen in the ASM data, though it is less obvious. To examine whether there is any difference in superorbital profile between regular and excursion epochs, we fold the light curve in both epochs (see bottom panel of Figure 3). The valley in the superorbital profile during the excursion epochs is shallower and narrower than that during the regular epochs. In contrast, the high-state count rate of the superorbital modulation profile in the excursion epochs is fully consistent with that in regular epochs, except for the *RXTE* ASM. To verify if the flux has long-term variability, we plot the evo-

**Table 3.** Spin Frequency of SMC X-1 Measured with Pointed X-Ray Observations.

MJD	Observatory	Spin Frequency (Hz)
55969.81	<i>Chandra</i>	1.425752(7)
57640.04	<i>XMM-Newton</i>	1.42941(3)
57650.35	<i>Swift</i>	1.4294(5)
57650.43	<i>XMM-Newton</i>	1.42943(3)
57685.58	<i>Swift</i>	1.429510(6)
57686.02	<i>XMM-Newton</i>	1.42951(3)

lution of the high- and low-state count rate in Figure 4. The energy ranges of these three data sets are quite different; hence, the count rate and the amplitude cannot be directly compared with each other. We estimate the *RXTE* ASM count rate after MJD 55400 by using of the MAXI GSC count rate. We fit the *RXTE* ASM count rate and MAXI GSC count rates in the overlapping epoch between MJD 55058 and MJD 55400 with a straight line and convert the MAXI count rate into the *RXTE* ASM count rate with the best-fit parameters.

The high-state count rate seems to drop during the first superorbital excursion event. Then, the count rate decays gradually until the second excursion. This trend could cause the high-state count rate difference between the superorbital profile in regular and excursion epochs with the ASM. The low-state count rate likely increases during the first excursion epoch and then fluctuates around zero. However, we could not exclude the possibility that the drop of the high-state count rate is a coincidence caused by a sudden flux increase event around MJD 51000. The high-state count rate seems stable after MJD 54000. In comparison, the low-state count rate increases during the excursion epochs. This suggests that the observed correlations in Figure 3 are dominated by the variability of the low-state count rate.

### 3.2. Spin Period Evolution

In this section, we search for the spin frequency with several new observations made with *Chandra*, *Swift* XRT, and *XMM-Newton*, as well as the photon events collected with the MAXI GSC. We first search for spin signal in pointed X-ray observations with the latest reported orbital ephemeris (Falanga et al. 2015). These measurements are used as cursors to perform a three-dimensional period search for MAXI GSC data (Section 3.2.3). We then use the measured  $90^\circ$  mean longitude ( $T_{\pi/2}$ , which is assumed to be the mid-eclipse time  $T_{\text{eci}}$ ), to refine the orbital ephemeris. Finally, we update the measurements from both the pointed observation and the MAXI GSC.



### 3.2.1. Algorithm of Spin Period Search

We employ the  $Z_2^2$  test to search for the spin period owing to the double-peaked pulse profile of SMC X-1 (Buccheri et al. 1983). The  $Z_2^2$  value for a trial frequency is

$$Z_2^2 = \left( \frac{2}{N_i} \right) \sum_{k=1}^2 \left[ \left( \sum_{j=1}^{N_i} \cos k\phi_j \right)^2 + \left( \sum_{j=1}^{N_i} \sin k\phi_j \right)^2 \right], \quad (5)$$

where  $N_i$  is the total number of photon events, and  $\phi_j$  is the phase of each photon calculated from the trial frequency. Assuming a pulsar with a steady spin-up rate over the time window for the spin period measurement, the spin frequency  $\nu(t)$  can be written as

$$\nu(t) = \nu_0 + \dot{\nu}(t - T_0), \quad (6)$$

where  $T_0$  is the zero epoch of the spin period measurement,  $\nu_0$  is the spin frequency at  $T_0$ ,  $\dot{\nu}$  is the time derivative of the spin frequency, and  $t$  is the arrival time of a photon. In a binary system, the orbital Doppler effect should be taken into account. Therefore, the phase can be calculated as

$$\begin{aligned} \phi_j = & \nu_0 \cdot (t_j - T_0) + \frac{1}{2} \dot{\nu} \cdot (t_j - T_0)^2 \\ & - \nu(t_j) \cdot \frac{a \sin i}{c} [\cos(2\pi\phi_{orb,t_j}) - \cos(2\pi\phi_{orb,T_0})] \\ & - \nu(t_j) \cdot \frac{a \sin i}{2c} e [\sin(4\pi\phi_{orb,t_j} - \Omega) - \sin(4\pi\phi_{orb,T_0} - \Omega)] \end{aligned} \quad (7)$$

where  $a$  is the semi-major axis of the binary orbit,  $i$  is the inclination angle,  $c$  is the speed of light,  $e$  is the eccentricity,  $\Omega$  is the periastron angle, and  $\phi_{orb,T_0}$  and  $\phi_{orb,t_j}$  are the orbital phases at  $t_j$  and  $T_0$ . For pointed X-ray observations, the  $\dot{\nu}$  term can be ignored owing to the short exposure. The best-determined spin period of all of the pointed observations with the updated orbital ephemeris (see Section 3.2.3) is summarized in Table 3.

### 3.2.2. Refinement of the Orbital Ephemeris

The photon events collected with the MAXI GSC provide a unique opportunity to track the spin and orbital period evolution in detail. During the entire  $\sim 9$  yr time span, the GSC collected  $\sim 1.2$  million X-ray photons in 2–20 keV within  $1^\circ$  of SMC X-1. We divide the observations into 65 segments, where each of them contains a full superorbital cycle. The incomplete cycles at the boundaries are neglected. In each segment, we search for the spin signal using photons collected during noneclipse epochs and  $\phi_{sup} = 0.1$ – $0.6$  to achieve a good signal-to-noise ratio. The total number of photons used in this analysis is  $\sim 0.6$  million, while the number of photons used in each segment varies between  $\sim 5000$  and  $\sim 18000$ .

We first search for the best triplet of  $\nu$ ,  $\dot{\nu}$ , and  $T_{\pi/2}$  in each superorbital cycle by assuming a circular orbit and

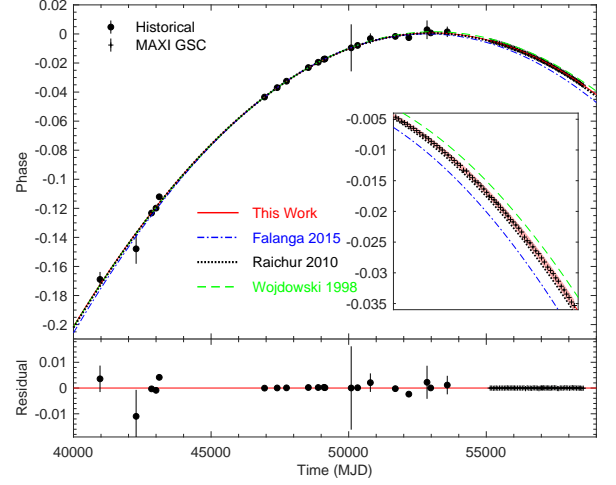


**Figure 5.** Arrival of the  $90^\circ$  mean longitude ( $T_{\pi/2}$ ) of SMC X-1. The best-fit quadratic ephemeris and three historical ephemerides are plotted (Wojdowski et al. 1998; Raichur & Paul 2010; Falanga et al. 2015). The embedded frame is the zoom-in view of the evolution after MJD 55000. The  $1\text{-}\sigma$  uncertainty interval of the best-fit model is shown as the red shaded area. The lower panel shows the residual.

freeze other orbital parameters to the values in Falanga et al. (2015). We start our search based on the segment between MJD 55952 and 56000 because it contains a precise spin measurement with *Chandra*. We search for frequencies near the best-determined value and  $\dot{\nu}$  from  $1 \times 10^{-11} \text{ s}^{-2}$  to  $4 \times 10^{-11} \text{ s}^{-2}$ . The oversampling factor is set to 10, i.e., 10 trial  $\nu$  within each peak with a Fourier width of  $\delta\nu = 1/2T$  where  $T$  is the time span of the segment. We also use the same oversampling factor for  $\dot{\nu}$ , i.e., 10 trial  $\dot{\nu}$  in the range of  $\delta\dot{\nu} = 1/T^2$ . For  $T_{\pi/2}$ , we use a 10 s resolution to search for the best values of  $\pm 2000$  s (corresponding to an orbital phase shift of 0.006) around the expected value predicted by Falanga et al. (2015). We then extend the search to all segments.

We find that the difference between the measured  $T_{\pi/2}$  and the expected value increases from  $\sim 400$  to  $\sim 1600$  s during the MAXI epoch. This implies a possible overestimate of the orbital period derivative in the orbital ephemeris. We therefore combine the historical measurements and the new  $T_{\pi/2}$  values to refine the orbital ephemeris.

The orbital phase evolution can be written as

$$\Delta\phi_{orb} = (\nu_{fold} - \nu_{orb}) \cdot (t - T_{\pi/2,0}) - \frac{1}{2} \dot{\nu}_{orb} (t - T_{\pi/2,0})^2, \quad (8)$$

where  $\nu_{fold}$  is the estimated orbital frequency at  $T_{\pi/2,0}$ ,  $\nu_{orb}$  is the corrected orbital frequency, and  $\dot{\nu}_{orb}$  is the time derivative of the orbital frequency. The orbital phases collected in Falanga et al. (2015) and the orbital phase calculated from the MAXI GSC data are presented in Figure 5. We fit the phase evolution with a

**Table 4.** Orbital Parameters and Corresponding  $1\sigma$  Uncertainties of SMC X-1.

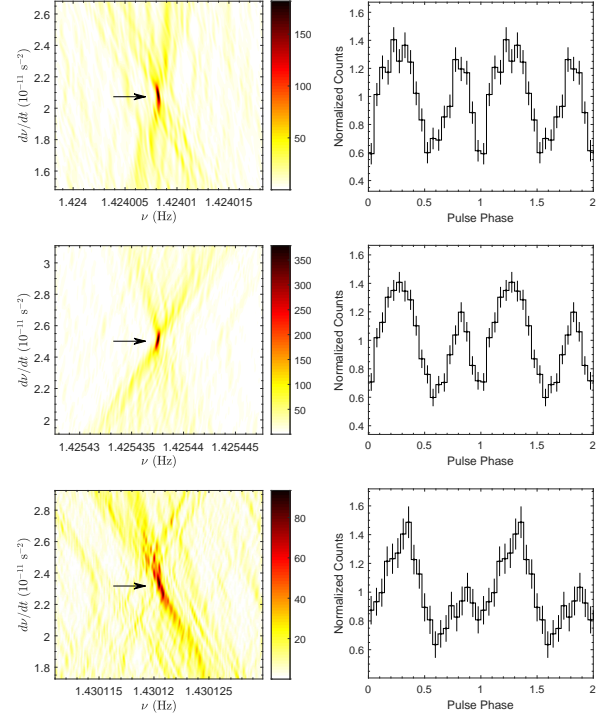
Parameter	Value
$T_{\pi/2,0}$	MJD 52846.6913(2)
Orbital period ( $P_{\text{orb}}$ )	3.8919297(2) days
$\dot{P}_{\text{orb}}/P_{\text{orb}}$	$-3.380(6) \times 10^{-6} \text{ yr}^{-1}$

quadratic curve using the robust statistic, which is designed to minimize the effect of outliers or influential observations by iteratively reweighting the least squares with a bisquare weighting function (Holland & Welsh 1977; Huber 1981). The best-fit parameter is shown in Table 4. A statistic of  $\chi^2_\nu = 14$  with a degree of freedom of 82 is obtained. We scale the measured  $1\sigma$  uncertainty by multiplying the value with the square root of  $\chi^2_\nu$  as a conservative estimate (see Table 4). The best-fit model is plotted in Figure 5. We plot the result from Wojdowski et al. (1998), Raichur & Paul (2010), and Falanga et al. (2015) for reference. All ephemerides seem to describe the data well, except for the MAXI observations. Our updated model is consistent with the ephemeris proposed by Raichur & Paul (2010) at a  $1\sigma$  level but deviates from that proposed by Wojdowski et al. (1998) and Falanga et al. (2015).

### 3.2.3. Two-dimensional Period Search with MAXI GSC

We then search for values of  $\nu$ ,  $\dot{\nu}$ ,  $T_{\pi/2}$ ,  $\Omega$ ,  $e$ , and  $a \sin i/c$  to maximize the  $Z^2_2$  value using the Nelder-Mead algorithm in each segment (Nelder & Mead 1965). From the best-determined value of the parameters in all segments, we find that  $a \sin i/c$  is well constrained as 53.48(2) lt-s. A finite eccentricity  $e = 0.0009(3)$ , and an  $\Omega = 10(40)^\circ$  are necessary. We freeze them and search for  $\nu$  and  $\dot{\nu}$  by using a two-dimensional  $Z^2_2$  test. All of the spin period measurements obtained with MAXI are listed in Table 7 of Appendix B. The uncertainties of  $\nu$  and  $\dot{\nu}$  are conservatively estimated from the width of the peak. The best-determined  $Z^2_2$  values vary between  $\sim 36$  and  $\sim 380$ . Three examples of the two-dimensional  $Z^2_2$  power spectra and the corresponding pulse profiles are shown in Figure 6. Most of the segments show a double-peaked profile in the 2–20 keV band where the peak height and valley depths are highly variable. On the other hand, a few segments (e.g., superorbital cycle 144) show a weak secondary peak similar to panel (f) of Figure 3 in Pike et al. (2019).

We plot all of the spin period measurements after MJD 50000, including the historical measurements from İnam et al. (2010) and Neilsen et al. (2004), *NuSTAR* data from Pike et al. (2019), and our measurements in Figure 7. The spin period of SMC X-1 increases monotonically, although short-term spin-down is possible (İnam et al.

**Figure 6.** (Left) Two-dimensional  $Z^2_2$  spectra near the best-determined spin frequency of SMC X-1 with MAXI GSC data in superorbital cycles 91, 103, and 144 (top to bottom). The arrow indicates the best-determined peak on the  $\nu$ - $\dot{\nu}$  plane. (Right) Corresponding normalized 2–20 keV pulse profile. Only photons collected between superorbital phases 0.1 and 0.6 are used in this analysis (see main text).

2010). The spin-up rate is, in contrast, highly variable. Compared to the long-term trend, SMC X-1 could have a higher spin-up rate during the first superorbital excursion epoch. This could be alternatively interpreted as the accretion torque having a putative change near the midpoint of the superorbital excursion or just a coincidence (Dage et al. 2019). By dividing the historical measurements into two segments according to MJD 50800, the spin-up rate changes from  $2.816(9) \times 10^{-11} \text{ s}^{-2}$  to  $2.520(6) \times 10^{-11} \text{ s}^{-2}$  (see Table 5). We find that neither the linear model nor the two-segment model can describe the spin period measurement after MJD 55000. Figure 7(a) shows the spin period measurements, while the residual after subtracting the best-fit linear trend using data points before MJD 53000 is plotted in Figure 7(b). We further fit the measurements after MJD 55000 with a straight line, yielding a spin-up rate of  $\dot{\nu} = 2.515(3) \times 10^{-11} \text{ s}^{-2}$ . This is consistent with the measurement from segment 50800–53000 but the spin frequency trends could not be connected well (see Figure 7(b)). We suggest a possible torque variability during the gap between *RXTE* and MAXI measurements, in which the second superorbital excursion event occurs. By fitting the data before MJD 53000 and after MJD

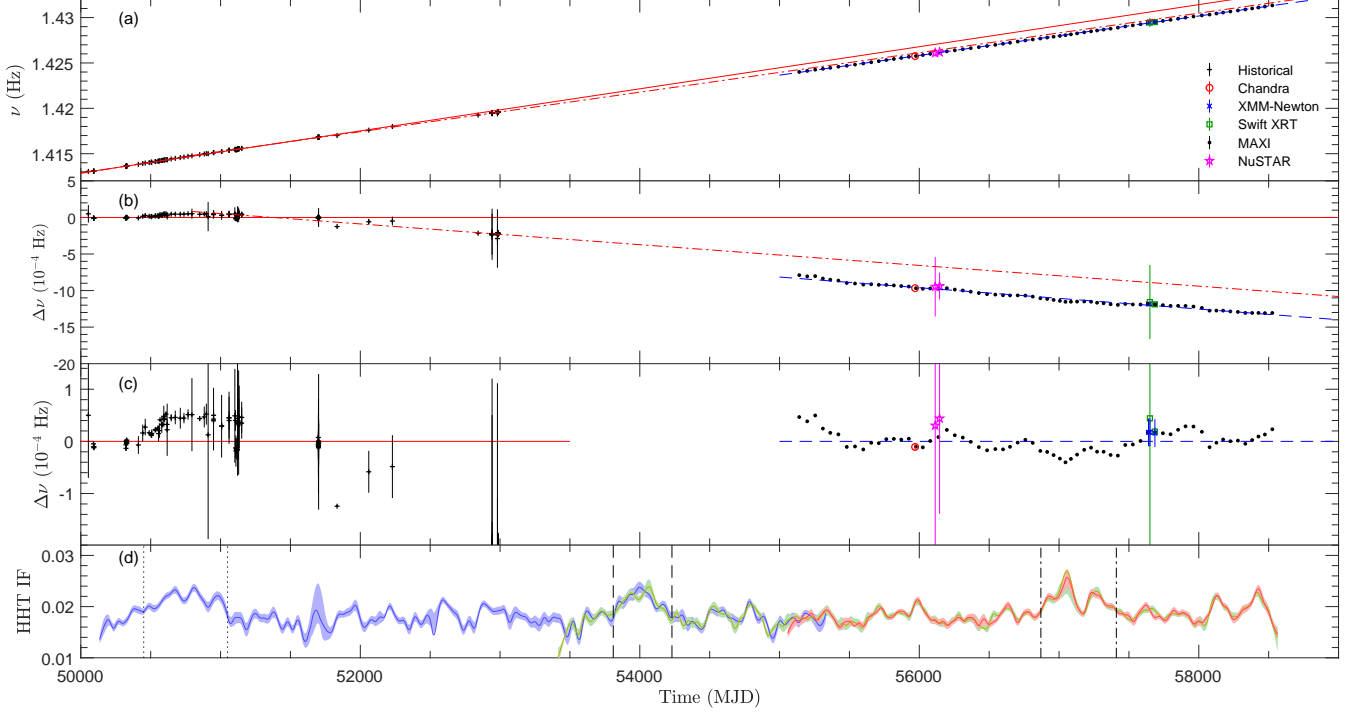


**Figure 7.** (a) Spin frequency evolution of SMC X-1 after MJD 50000. The red solid line denotes the best-fit linear model with data points before MJD 53000. The red dashed-dotted line denotes the best-fit linear model with data points between MJD 50800 and MJD 53000. The blue dashed line denotes the linear model with data points collected after MJD 55000. (b) Frequency residual after subtracting the best-fit linear model with data before MJD 53000. (c) Frequency residual after separately fitting the data in MJD 50000–53000 and MJD 55000–59000 with straight lines. (d) Instantaneous superorbital frequencies obtained with the *RXTE* ASM, *Swift* BAT, and MAXI GSC. The color notations and auxiliary lines are defined in the same manner in Figure 1

55000 separately, the corresponding residuals are plotted in Figure 7(c). The instantaneous superorbital frequency is shown in panel (d) for reference.

The spin frequency evolution obtained with the MAXI GSC shows no positive correlation with the superorbital frequency. Instead, the minimum coincides with the excursion epoch of the superorbital modulation frequency. A correlation analysis between the frequency residual and the instantaneous superorbital frequency suggests a weak anticorrelation with  $\tau_k = -0.23$  and  $p = 8 \times 10^{-3}$  (Figure 8). We use the bootstrap algorithm to perform  $10^6$  simulations and obtain  $\tau_k = -0.29 \pm 0.08$  with a probability of  $1.2 \times 10^{-3}$  showing a positive  $\tau_k$ . This apparent correlation could be dominated by the of a sudden change in the spin frequency during the major superorbital excursion. By dividing the spin frequency measurement into two segments according to  $\sim$ MJD 57050, the spin-up rate changes from  $2.489(5) \times 10^{-11} \text{ s}^{-2}$  to  $2.544(7) \times 10^{-11} \text{ s}^{-2}$ .

### 3.3. Orbital Profile Variability

The complex and variable orbital profile of SMC X-1 provides hints of the emission and absorption geometries of this system. Trowbridge et al. (2007) discovered a “bounce-back” feature during the eclipse with a soften-

**Table 5.** Local Spin-up Rate of SMC X-1.

MJD Range	$\dot{\nu}$ ( $10^{-11} \text{ s}^{-2}$ )
50098–52988	2.684(3)
50098–50800	2.816(9)
50800–52988	2.520(6)
55141–58526	2.515(3)
55141–57050	2.489(5)
57050–58526	2.544(7)

ing and a sinusoidal profile during the noneclipse phases by observing the averaged orbital profile with the *RXTE* ASM. Hu et al. (2013) further divided the ASM data into four superorbital states and found a possible hint of pre-eclipse dips. We reexamine the orbital profile variability with respect to the superorbital phase using *Swift* BAT and MAXI GSC data. The orbital profiles in the four superorbital states are shown in Figure 9. The bounce-back feature cannot be seen. A sinusoidal-like modulation can be observed in the superorbital ascending,

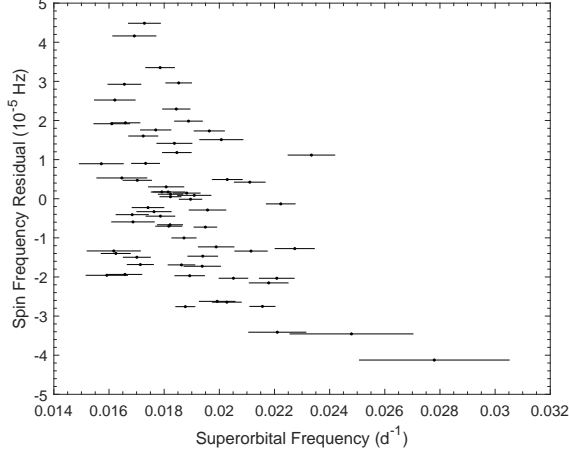


**Figure 8.** Spin period residual versus superorbital frequency.

descending, and low states, but the X-ray flux during the post-eclipse phases ( $\phi_{\text{orb}} \sim 0.1\text{--}0.5$ ) is likely higher than that during the pre-eclipse phases ( $\phi_{\text{orb}} \sim 0.5\text{--}0.9$ ). Moreover, a dip-like feature at  $\phi_{\text{orb}} \sim 0.7\text{--}0.8$  can be observed with all three satellites, especially in the superorbital descending state.

We calculate the HR profile using the definition in Equation 4 for the first two MAXI GSC energy bands (see Figure 10). The HR values during the eclipse contain huge error bars; thus, we remove them from the plot. In general, the HR varies between 0.1 and 0.4 during the noneclipse phases. We do not observe clear spectral variability corresponding to the sinusoidal profile. A hardening feature is marginally seen at  $\phi_{\text{orb}} \sim 0.7\text{--}0.8$  during the superorbital transition states, although the uncertainty is large. This HR change is not seen in the averaged orbital profile obtained with the ASM (see, e.g., Figure 3 of Trowbridge et al. 2007) and could be caused by both the insufficient photon statistic of ASM and the superorbital dependence of the dip.

### 3.4. Superorbital and Orbital Profiles in the Optical Band

The orbital modulation of SMC X-1 can be seen in the optical band with the OGLE survey data (Udalski 2003; Coe et al. 2013). Moreover, the superorbital modulation is also weakly determined. We try to use the archival ASAS-SN data to see if the optical modulation can be independently obtained with a different survey program. We fold the light curve according to the orbital ephemeris and find that the orbital modulation can be seen in both the *V* and *g* bands (Figure 11). The optical profile is double-peaked, likely caused by the ellipsoidal modulation of a Roche lobe filling companion star. Similar to the result obtained in Coe et al. (2013), the flux minimum at  $\phi_{\text{orb}} = 0.5$  is brighter than that at  $\phi_{\text{orb}} = 0$ ,

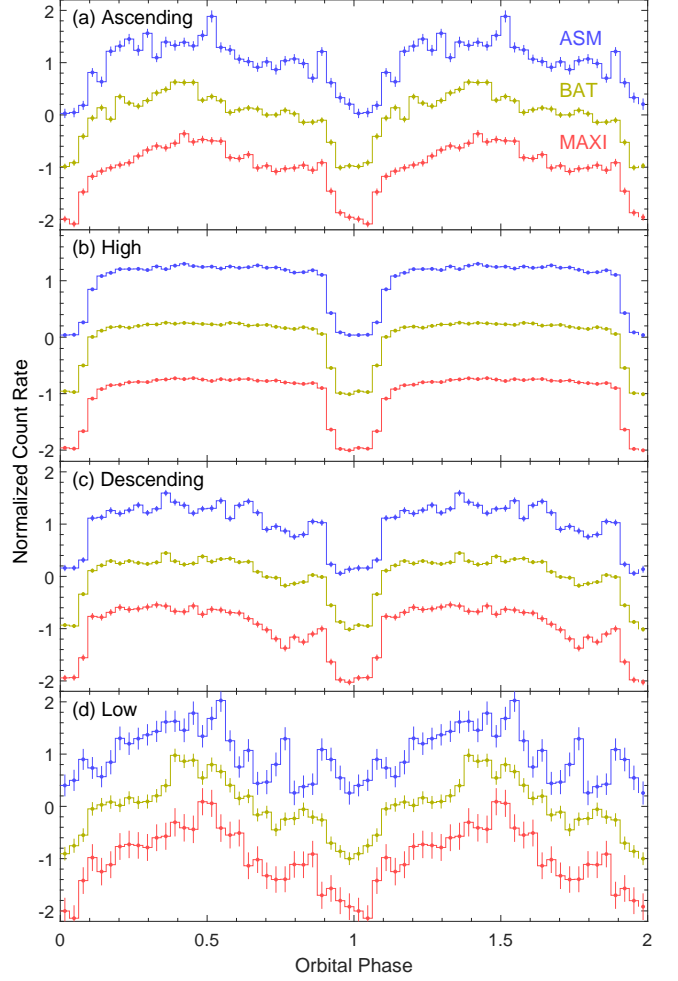


**Figure 9.** Orbital profile of SMC X-1 observed in (a) the ascending state, (b) the high state, (c) the descending state, and (d) the low state. Profiles obtained from the *RXTE* ASM, *Swift* BAT, and MAXI GSC are ordered from top to bottom with an offset of  $-1$  in each panel.

which is a feature of X-ray heating of the companion's surface (Rawls et al. 2011).

We then attempt to fold the light curves according to the superorbital phase defined with the HHT but fail to obtain a significant modulation profile. This could be caused by the contamination of the strong orbital modulation because only  $\sim 3\%$  of the optical emission is expected to modulate at the superorbital period (Coe et al. 2013). Therefore, we create a template by smoothing the orbital profile. Then, we get the residual magnitude of each observation by subtracting the template from the observed magnitude. The residual has an RMS scattering of 0.04 mag in the *V* band and 0.02 mag in the *g* band. We fold the residual light curve according to the superorbital phase and obtain superorbital profiles (Figure 11). Both the *V*- and *g*-band profiles show a clear modulation with a valley at  $\phi_{\text{sup}} \approx 0.7\text{--}1$ . The peak-to-peak amplitudes of the *V*- and *g*-band



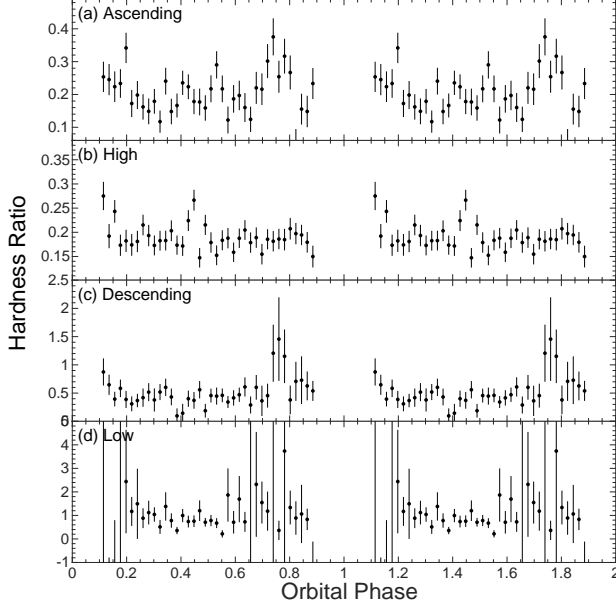


**Figure 10.** The HR versus orbital phase of SMC X-1 observed in (a) the ascending state, (b) the high state, (c) the descending state, and (d) the low state.

superorbital profiles are  $\sim 0.02$  and  $\sim 0.025$  mag, respectively. We further obtain the superorbital profile using the data collected in MJD 58002–58385, where SMC X-1 is simultaneously observed with both the  $V$  and  $g$  bands although the observational cadences between these two bands are different. The result is fully consistent with that observed from the entire data set.

#### 4. DISCUSSION

##### 4.1. Implication of Superorbital Period Excursion

For the first time, we extend the study of the superorbital modulation to  $\sim 7$  yr after the end of the *RXTE* mission. A new major superorbital excursion event is observed independently with the *Swift* BAT and MAXI GSC near  $\sim$ MJD 57100. This suggests that the superorbital excursion event could have a (quasi)periodicity of  $\sim 3100$ – $3200$  days, which confirms the prediction made by Hu et al. (2011). If this is true, a period excursion is expected to occur at  $\sim$ MJD 47600. Unfortunately, the *BATSE* observation does not cover this epoch, but a possible fluctuation in  $f_{\text{sup}}$  can be seen before  $\sim$ MJD 49000 (Clarkson et al. 2003).

The instantaneous frequencies obtained with the *RXTE* ASM, *Swift* BAT, and MAXI GSC have moderate differences near the boundaries of individual data sets. The discrepancies are caused by the end effect of the EMD that leads to low robustness in the instantaneous frequency measurements. Except for the boundaries, the instantaneous frequencies observed by different satellites are generally consistent with each other. This indicates that not only the excursion events

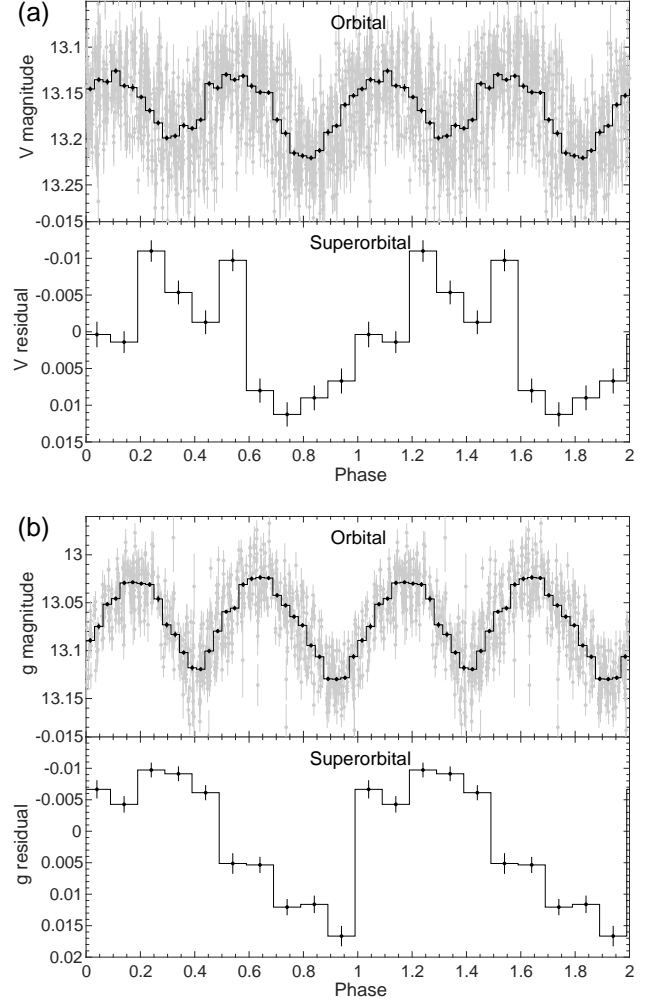


**Figure 11.** The ASAS-SN folded light curves in the (a)  $V$  and (b)  $g$  band. The gray points in the upper panel of each figure are magnitude measurements versus orbital phase, where the histogram shows the average orbital profile with 32 bins. The lower panel shows the superorbital profile of the residual after removing the orbital modulation.

described in the previous paragraph but also the short-term variabilities are intrinsic features of SMC X-1. These minor fluctuations have been noticed in (Hu et al. 2011) solely using the *RXTE* ASM. For example, the superorbital frequency showed a double-peaked feature near  $\sim 54200$ – $54500$ . This event is clearly seen regardless of the analysis techniques (WWZ and HHT) and the observation instrument (*RXTE* ASM and *Swift* BAT). Similar events are also seen in  $\sim$ MJD 52200–52500 and  $\sim$ MJD 55200–55500.

A possible hint of a weak correlation between the superorbital modulation period and modulation amplitude is observed (Hu et al. 2011). We confirm that during the excursion epoch, the superorbital profile has a low am-

plitude, which is dominated by the increase of low-state flux.

The current leading model of the superorbital modulation is the occultation by a precessing and warped disk (Wijers & Pringle 1999; Ogilvie & Dubus 2001). Such a warp could be driven by the perturbation from the strong radiation (Petterson 1977; Pringle 1996; Wijers & Pringle 1999). The stability of the warp is characterized by the binary separation ( $r_b$  in units of  $GM_{\text{NS}}/c^2$ ) and  $q$ . A large  $r_b/q$  value suggests a highly unstable warp mode (Ogilvie & Dubus 2001). Both stable mode 0 and unstable mode 1 precession could be contained in SMC X-1 and hence cause the drift of the superorbital modulation period (Clarkson et al. 2003; Charles et al. 2008).

The disk warp model predicts a connection between the disk luminosity and the superorbital modulation period as

$$P_{\text{sup}} \sim \frac{\Sigma_d R_d^{3/2}}{L_d}, \quad (9)$$

where  $\Sigma_d$  is the surface density of the disk,  $R_d$  is a characteristic radius of the disk, and  $L_d$  is the strength of the radiation field from the disk (Wijers & Pringle 1999; Still & Boyd 2004). However, the decreasing trend of the high-state flux between the first and the second excursion events does not result in an increasing trend of the superorbital cycle length. This implies that the mass accretion rate is not strongly associated with the superorbital period.

Owing to the low inclination angle ( $i = 65^\circ$ ; Val Baker et al. 2005) of SMC X-1, the increment in the low-state flux during the excursion epochs can be interpreted as the decrease of warp because the emission near the neutron star may not be fully obscured during the superorbital low state. The warp angle is expected to vary with time quasiperiodically or aperiodically, although its connection to the precession period remains unclear (Pringle 1997). Furthermore, the gradual change of the hardness ratio during the superorbital transition state suggests that the atmosphere of the disk is not fully opaque. Variability in the warp angle could change the obscuring percentage of the X-ray emission and the optical depth along the line of sight during the superorbital transition and low states. This results in the variability of the low-state flux as seen in our analysis.

Utilizing the ASAS-SN data, we independently obtain the superorbital modulation profile in the optical band (see Figure 11). The peak-to-peak amplitude of the superorbital modulation roughly corresponds to a 2.3% flux difference, in the same order as that obtained by Coe et al. (2013) by using the OGLE data. The optical profile is in phase with the X-ray superorbital profile, implying that the superorbital modulation in the optical band is from the same source as the superorbital modulation in the X-ray band. The optical emission from the disk is believed to be the reprocessed X-ray

(Howarth 1982). A global warp of the disk with a maximum disk warp angle at the edge and with a finite tilt angle could interpret the observational result (Foulkes et al. 2010). During the superorbital low state, the X-ray-illuminated side of the disk is partially obscured by the backlight side of the warp. The presence of the superorbital phase-dependent pre-eclipse dip also suggests a deviation of the outermost disk from the orbital plane. During the superorbital high state, the near side of the outer disk is far from our line of sight; hence, the bulge could not pass through our line of sight. Given that the accretion disk contributes  $\sim 5\%$  of the optical emission (Howarth 1982), roughly 40% of the disk emission in the optical band is obscured during the superorbital low state.

Alternatively, the companion star could be heated by the neutron star, and the warped disk could cause a shadow on the companion. This could drive the superorbital modulation in the optical band and change the orbital profile along with the superorbital phase (see, e.g., Deeter et al. 1976; Gerend & Boynton 1976). However, the superorbital modulation in the optical band would be more likely be out of phase with the X-ray modulation. This is not consistent with the observation but could be an origin that reduces the observed optical modulation amplitude.

#### 4.2. Spin-Superorbital Connection

The high time resolution and the large effective area of the MAXI GSC allow us to track the spin period of SMC X-1 and refine the orbital parameters. We find that  $a \sin i/c$ ,  $e$ , and  $\Omega$  are not well constrained compared to several pointed observations (see, e.g., Raichur & Paul 2010). Moreover, their values are not consistent with each other from different measurements (Inam et al. 2010; Raichur & Paul 2010). This could be caused by the variability of the pulse profile (Raichur & Paul 2010). Previous observations suggest that the pulse profile of SMC X-1 only varies dramatically in the soft X-ray band (Neilsen et al. 2004; Hickox & Vrtilek 2005) but recent *NuSTAR* observations suggest that the profile is likely superorbital phase-dependent in the hard X-ray (Pike et al. 2019). Our study shows that the averaged pulse profile varies between superorbital cycles in the 2–20 keV band (see Figure 6). This could be originated not only from the intrinsic variability of the pulse profile but also from the variability of  $\dot{\nu}$  within one superorbital cycle. In a few superorbital segments that result in a high  $Z_2^2$  values, we find that  $\nu$  has a clear drift with a variable  $\dot{\nu}$  rate. This could distort the pulse profile if we assume a fixed  $\dot{\nu}$  within a superorbital cycle. Nevertheless, these two effects prevent us from measuring a precise orbital eccentricity and the angle of periastron.

It is suggested that the spin period evolution of SMC X-1 could have a connection to the variability of the superorbital modulation (Dage et al. 2019). We do not observe a clear positive correlation between superor-

bital frequency and the spin frequency residual with the MAXI GSC and hence suggest that the apparent correlation observed with *RXTE* could be a coincidence.

The spin-up rate of an accreting pulsar is dominated by the change of mass accretion rate. The spin-up torque ( $N$ ) is expressed as

$$N \approx \dot{M} \sqrt{GM_{\text{NS}} r_m}, \quad (10)$$

where  $\dot{M}$  is the mass accretion rate,  $M_{\text{NS}}$  is the mass of the neutron star, and  $r_m$  is the magnetospheric radius. The value of  $r_m$  also depends on  $\dot{M}$  as

$$r_m \propto \left( \frac{\mu^4}{M_{\text{NS}} \dot{M}^2} \right)^{\frac{1}{7}}, \quad (11)$$

where  $\mu$  is the magnetic moment of the neutron star (Pringle & Rees 1972; Ghosh & Lamb 1979; Bildsten et al. 1997). When  $r_m$  is smaller than the corotating radius, the neutron star spins up with a rate positively correlated with the mass accretion rate. If this is the case for SMC X-1, a correlation between the spin-up rate and the high-state flux is expected. We do not observe a clear flux increase during the first superorbital excursion; hence, the spin period change is likely not caused by the change of the mass accretion rate. The X-ray flux between the first excursion epoch and the second excursion epochs likely has a decreasing trend (Figure 4). This could result in a decrease in the spin-up trend and partly cause the overestimate of the frequency after MJD 55000 by fitting spin period measurements in MJD 50800–53000 with a straight line.

On the other hand, the angular momenta of the materials on a warped disk also depend on the warp angle. If the excursion of the superorbital period is caused by the instability of the warp, a connection between the spin-up rate change and the superorbital modulation period is expected. This could be tested using MAXI GSC data because the high-state flux during MAXI observations is relatively stable. We indeed observe a hint of anticorrelation that is inconsistent with the behavior observed with *RXTE* near the first superorbital excursion event (see Section 3.2.3).

However, the apparent anticorrelation could be a coincidence. The superorbital period excursion could permanently change the disk configuration, and the warp inclination may not exactly return to the pre-excursion value. This could cause a sudden change of accretion torque as suggested in Dage et al. (2019) although a time lag between the spin period change and superorbital period excursion is possible. If this is true, the third superorbital period excursion event increases the accretion torque. This is different from that in the first superorbital period excursion event. Moreover, the torque could also be changed during the minor excursion events of the superorbital period. Several minor superorbital excursion events coincide with the local minima of the spin

period residual (see Figure 7), but a few peaks of the superorbital frequency are likely with the local maxima of the frequency residual. Therefore, the apparent anticorrelation during the MAXI GSC observation could be a biased effect if we observe more minor excursion events associated with positive torque changes than those events associated with negative changes.

The spin period evolution of SMC X-1 is complicated and could be associated with the change of the mass accretion rate and the variability of the warp angle. Therefore, we could not obtain a global correlation between the superorbital and spin frequencies. Our result suggests that the excursion in the superorbital modulation period could change the accretion torque, but the size and the direction of change remain unclear. Therefore, we could not entirely exclude the possibility that the spin period evolution is unassociated with the change of the superorbital period. Monitoring the spin and superorbital behaviors of SMC X-1 would be helpful to probe the spin-superorbital connection.

#### 4.3. Comparison to Her X-1

Similar to SMC X-1, Her X-1 is a famous X-ray binary that shows fruitful irregularities in the superorbital modulation amplitude and pulse profile and a connection between spin and superorbital modulation. Her X-1 shows a positive correlation between the superorbital period and ASM flux at main-on, not consistent with Equation 9 (Still & Boyd 2004; Leahy & Igna 2010). Her X-1 is argued to have a luminosity higher than the threshold value that causes the self-occultation of the disk. Strong emission from the neutron star effectively reduces the radiation pressure and increases the superorbital period (Still & Boyd 2004). Different from Her X-1, our result shows that the correlation between modulation amplitude and superorbital cycle length is dominated by the low-state flux, which is not directly associated with the mass accretion rate and the disk luminosity. The direct observational evidence is that the pulse profile of Her X-1 at all energies varies with the superorbital cycle (Scott et al. 2000; Staubert et al. 2013), while for SMC X-1, the pulse profile only varies at soft energies (Hickox & Vrtilek 2005), although recent *NuSTAR* observations show that the pulse profile of SMC X-1 is also moderately variable in the hard X-ray (Pike et al. 2019).

The spin period of Her X-1 does not monotonically increase with time. It occasionally spins down when the main-on flux is low. The pulsar in Her X-1 significantly spins down during the anomalous low states, in which the superorbital modulation cannot be seen (see, e.g., Staubert et al. 2009, and the *Fermi* GBM pulsar monitoring program<sup>3</sup>). It is suggested that the warp angle of the innermost accretion disk could be higher than 90°

<sup>3</sup> <https://gammaray.msfc.nasa.gov/gbm/science/pulsars.html>

and result in a spin-down torque during the anomalous low state (Parmar et al. 1999). The orbital profile of Her X-1 in the optical band is found to vary over the superorbital phase (Deeter et al. 1976; Gerend & Boynton 1976). However, the orbital profile at any specific superorbital phase, as well as the superorbital profile in the optical band, remain consistent between the normal state and the anomalous low state (Jurua et al. 2011). This suggests that the change of the disk warp is very slight between these two states. Another explanation is that the decrease of the mass accretion rate enlarges the magnetospheric radius to be larger than the corotating radius (Leahy & Igna 2010). The accretion is then prohibited due to the centrifugal barrier and causes the pulsar spin down. We do not observe a significant spin-down torque in SMC X-1; hence, we suggest that SMC X-1 remains far from the equilibrium and the change in warp angle is not extremely strong.

#### 4.4. Precession of a Ring Tube

The superorbital profile of SMC X-1 could also be modeled by the tidal-induced precession of a tilted disk, where the X-ray is quasiperiodically obscured by the ring tube on the disk (Inoue 2012, 2019). This model can reproduce the light-curve shape of SMC X-1, LMC X-4, and Her X-1. The geometrically thick ring is formed at the outermost part of the accretion disk with a radius of

$$\frac{R_{\text{ring}}}{a} = \left[ 2 \frac{(1+q)^{1/2}}{q} \frac{P_{\text{orb}}}{P_{\text{sup}}} \frac{1}{\cos \theta} \right]^{2/3}, \quad (12)$$

where  $R_{\text{ring}}$  is the radius of the ring, and  $\theta$  is the tilt angle of the ring axis against the precession axis. For SMC X-1, this value is  $\sim 0.13$ . In this model, the warp of the disk is negligibly small (Inoue 2012). The variability of the low-state flux varies due to the change of the opacity of the ring tube, the scale height of the tube, and the tilt angle of the disk. The scale height  $x_0$  of the ring tube can be described as

$$x_0 = \left( \frac{2kT}{m_H G M_{\text{NS}}} \right)^{\frac{1}{2}} R_{\text{ring}}^{\frac{3}{2}}, \quad (13)$$

where  $T$  is the disk temperature,  $m_H$  is the mass of a hydrogen atom,  $k$  is the Stefan-Boltzmann constant and  $G$  is the gravitational constant. The relation between  $T$  and the ionization parameter  $\xi$  is  $T \propto \xi^\eta$  where  $\eta$  is a logarithmic slope. Assuming a constant X-ray luminosity  $L_X$ , this relation can be written as

$$T \propto (n_0 R_{\text{ring}}^2)^{-\eta}, \quad (14)$$

where  $n_0$  is the gaseous number density at the tube center. According to the mass conservation  $n_0 x_0^2 R_{\text{ring}} = \text{constant}$ , we can derive

$$x_0 \propto R_{\text{ring}}^{(3+\eta)/2(1-\eta)} \quad (15)$$

Moreover, the optical depth  $\tau_0$  of the ring tube is evaluated as  $\tau_0 = \sigma_T n_0 x_0$ , where  $\sigma_T$  is the Thompson cross section. We can then calculate the relationship between  $\tau_0$  and  $R$  as

$$\tau_0 \propto R_{\text{ring}}^{(1+3\eta)/2(1-\eta)} \propto P_{\text{sup}}^{-(1+3\eta)/3(1-\eta)}. \quad (16)$$

As long as  $\eta > 1$ , the optical depth and the scale height of the tube decrease as  $P_{\text{sup}}$  decreases. This increases the low-state flux and reduces the superorbital amplitude. However, the tilt angle increases as  $R_{\text{ring}}$  by  $\delta R_{\text{ring}}/R_{\text{ring}} \propto \tan \theta \delta \theta$  where  $\theta$  is the tilt angle of the disk (Inoue 2012). This increases the obscuring/absorption ratio of the X-ray emission and enhances the observed amplitude. The viewing geometry has to be strongly restricted to reproduce the observed anticorrelation.

The superorbital modulation in the optical band is expected if the emission from the ring is mainly in the optical band. Finally, the connection between the evolution of the spin period and the superorbital modulation could also be interpreted, since the tilt angle of the disk changes with the superorbital modulation period.

## 5. SUMMARY

In this research, we track the evolution of the superorbital period in SMC X-1 with the *RXTE* ASM, *Swift* BAT, and MAXI GSC with a baseline longer than 23 yr. With the high-quality MAXI GSC data, we also study the HR variability, along with the orbital and superorbital phases, and track the spin period evolution. Our achievements and conclusions are as follows.

(i) Three major superorbital excursion events are identified at  $\sim$ MJD 50800, 54000, and 57100. Several minor excursions are seen during the regular epochs between major excursion events. We suggest that the excursion event is likely recurrent and possible (quasi)periodic.

(ii) We observe a gradual change of the HR during the superorbital transition state, implying a possible absorption. This could be interpreted if the atmosphere of the warped disk is not entirely opaque.

(iii) From the correlation analysis, we find that the low-state flux increases during the excursion epoch. In contrast, the high-state flux shows less obvious variation, except for the first excursion. This indicates that the X-ray emission from the central region is not fully obscured/absorbed during the excursion epoch.

(iv) A gradual decrease in the high-state flux is found during MJD 51500 and 53500, where no significant trend in the superorbital modulation period is found. We suggest that the change in the superorbital modulation period is not dominated by the mass accretion rate.

(v) We successfully track the spin period evolution with a sequence of two-dimensional period searches on MAXI GSC data. We do not observe a positive correlation between the superorbital frequency and the spin period evolution. On the other hand, a possible weak



anticorrelation is observed. This could be interpreted if the major/minor excursion events result in a change of the accretion torque.

(vi) We refine the orbital ephemeris according to the spin period measurement with the MAXI GSC.

(vii) An increase in the HR at  $\phi_{\text{orb}} = 0.7\text{--}0.8$  is marginally seen during the superorbital descending state. This supports the idea that SMC X-1 is a dipping HMXB.

(viii) We reconfirm the superorbital modulation in the optical band with ASAS-SN data. The superorbital profile in the optical band is in phase with the X-ray one.

(ix) The ring tube on a precessed and tilted accretion disk provides an alternative interpretation for the superorbital modulation. The observed phenomena could be explained by the change of tilt angle, opacity, and scale height of the ring tube.

We thank Prof. Hajime Inoue for useful discussions. We appreciate valuable comments from the referee to improve this paper. This work made use of data provided by the ASM/*RXTE* teams at MIT and the *RXTE* SOF and GOF at NASA's GSFC, the *Swift* BAT data provided by the hard X-ray transient monitor (Krimm et al. 2013), and the MAXI data provided by RIKEN, JAXA, and the MAXI team. This work also made use *Swift* XRT data supplied by the UK Swift Science Data Centre at the University of Leicester and *Chandra* data obtained from the *Chandra* Data Archive. We also made use of observations made with *XMM-Newton*, which is an ESA science mission with instruments and contributions directly funded by the ESA member states and NASA. C.-P.H. acknowledges support from the Japan Society for the Promotion of Science (JSPS; ID: P18318).

*Facilities:* *RXTE* (ASM), *Swift* (XRT, BAT), MAXI (GSC), *CXO* (HRC), *XMM* (PN)

*Software:* CIAO (Fruscione et al. 2006), *XMM-Newton* SAS, HEASoft

## APPENDIX

### A. MEASUREMENTS OF SUPERORBITAL MINIMA

We list the arrival times of the superorbital minimum obtained with *RXTE* ASM, *Swift* BAT, and MAXI in Table 6. The corresponding high- and low-state count rates for the correlation analysis are also included.

**Table 6.** Arrival time of superorbital minima and corresponding high- and low-state count rate measured with ASM, BAT, and MAXI.

Cycle	<i>RXTE</i> ASM			<i>Swift</i> BAT			MAXI GSC		
	$T_{\text{min}}^a$	High <sup>b</sup>	Low <sup>c</sup>	$T_{\text{min}}^a$	High <sup>b</sup>	Low <sup>c</sup>	$T_{\text{min}}^a$	High <sup>b</sup>	Low <sup>c</sup>
1	50191.9(8)	...	...	...	...	...	...	...	...
2	50191.9(8)	2.95(6)	0.26(8)	...	...	...	...	...	...
3	50252.5(7)	3.56(5)	0.27(6)	...	...	...	...	...	...
4	50312.4(4)	2.96(8)	0.22(8)	...	...	...	...	...	...
5	50368.2(6)	2.97(7)	0.35(13)	...	...	...	...	...	...
6	50418.6(7)	3.31(6)	0.40(9)	...	...	...	...	...	...
7	50473.2(6)	2.29(8)	0.48(14)	...	...	...	...	...	...
8	50519.5(8)	2.89(9)	0.09(10)	...	...	...	...	...	...
9	50572.1(6)	2.93(9)	0.41(11)	...	...	...	...	...	...
10	50617.7(6)	2.54(6)	0.71(7)	...	...	...	...	...	...
11	50662.5(6)	2.81(10)	0.17(10)	...	...	...	...	...	...
12	50705.3(5)	3.00(17)	0.57(13)	...	...	...	...	...	...
13	50752.1(7)	2.79(6)	0.82(9)	...	...	...	...	...	...
14	50798.0(6)	2.67(13)	0.76(16)	...	...	...	...	...	...

Table 6 continued

**Table 6** (*continued*)

Cycle	<i>RXTE</i> ASM			<i>Swift</i> BAT			MAXI GSC		
	$T_{\min}^a$	High <sup>b</sup>	Low <sup>c</sup>	$T_{\min}^a$	High <sup>b</sup>	Low <sup>c</sup>	$T_{\min}^a$	High <sup>b</sup>	Low <sup>c</sup>
15	50839.6(6)	2.72(12)	-0.14(13)	...	...	...	...	...	...
16	50886.5(6)	2.66(12)	0.20(9)	...	...	...	...	...	...
17	50935.5(8)	2.39(6)	0.12(12)	...	...	...	...	...	...
18	50981.5(7)	2.67(8)	0.56(10)	...	...	...	...	...	...
19	51028.5(7)	3.17(13)	0.30(15)	...	...	...	...	...	...
20	51086.4(13)	2.63(11)	-0.15(14)	...	...	...	...	...	...
21	51141.9(8)	2.97(10)	0.40(15)	...	...	...	...	...	...
22	51203.7(9)	3.26(15)	0.20(12)	...	...	...	...	...	...
23	51258.3(7)	2.82(7)	0.28(6)	...	...	...	...	...	...
24	51314.1(6)	3.39(7)	0.35(9)	...	...	...	...	...	...
25	51370.1(7)	3.33(11)	0.13(7)	...	...	...	...	...	...
26	51424.5(7)	3.01(7)	0.31(9)	...	...	...	...	...	...
27	51485.3(6)	2.93(6)	0.01(10)	...	...	...	...	...	...
28	51548.5(4)	2.96(8)	0.56(21)	...	...	...	...	...	...
29	51614.7(20)	2.84(12)	0.04(12)	...	...	...	...	...	...
30	51673.8(11)	2.18(7)	0.13(10)	...	...	...	...	...	...
31	51739.0(7)	2.78(7)	0.17(16)	...	...	...	...	...	...
32	51803.1(8)	2.94(5)	0.15(11)	...	...	...	...	...	...
33	51859.6(6)	2.94(5)	0.29(13)	...	...	...	...	...	...
34	51912.9(7)	2.72(12)	-0.01(10)	...	...	...	...	...	...
35	51964.7(7)	2.80(19)	0.32(8)	...	...	...	...	...	...
36	52017.7(12)	3.05(5)	0.17(9)	...	...	...	...	...	...
37	52078.7(5)	2.95(4)	0.38(20)	...	...	...	...	...	...
38	52137.3(6)	2.63(4)	0.18(8)	...	...	...	...	...	...
39	52193.7(8)	3.19(9)	0.17(10)	...	...	...	...	...	...
40	52243.6(7)	3.07(8)	-0.02(11)	...	...	...	...	...	...
41	52301.0(7)	2.64(10)	0.40(12)	...	...	...	...	...	...
42	52364.1(12)	2.18(10)	0.32(9)	...	...	...	...	...	...
43	52418.3(7)	3.04(6)	0.09(7)	...	...	...	...	...	...
44	52478.5(5)	2.26(7)	0.43(14)	...	...	...	...	...	...
45	52545.4(4)	2.64(6)	0.12(14)	...	...	...	...	...	...
46	52594.7(6)	2.58(6)	0.18(13)	...	...	...	...	...	...
47	52643.3(7)	2.49(9)	0.20(13)	...	...	...	...	...	...
48	52695.6(9)	2.42(10)	0.07(10)	...	...	...	...	...	...
49	52757.8(6)	2.79(7)	0.13(10)	...	...	...	...	...	...
50	52818.5(12)	2.51(6)	0.17(9)	...	...	...	...	...	...
51	52871.9(6)	3.02(10)	0.00(5)	...	...	...	...	...	...

*Table 6 continued*

Table 6 (continued)

Cycle	RXTE ASM			Swift BAT			MAXI GSC		
	$T_{\min}^a$	High <sup>b</sup>	Low <sup>c</sup>	$T_{\min}^a$	High <sup>b</sup>	Low <sup>c</sup>	$T_{\min}^a$	High <sup>b</sup>	Low <sup>c</sup>
52	52921.6(6)	2.47(8)	0.12(7)	...	...	...	...	...	...
53	52972.1(6)	2.28(6)	0.25(17)	...	...	...	...	...	...
54	53025.0(7)	3.24(10)	0.45(19)	...	...	...	...	...	...
55	53082.5(16)	2.11(11)	0.16(6)	...	...	...	...	...	...
56	53135.4(8)	2.44(9)	0.09(8)	...	...	...	...	...	...
57	53190.0(6)	2.73(10)	-0.04(9)	...	...	...	...	...	...
58	53249.0(7)	2.73(5)	0.14(16)	...	...	...	...	...	...
59	53308.4(6)	2.48(4)	-0.02(10)	...	...	...	...	...	...
60	53365.7(8)	2.42(11)	0.05(11)	...	...	...	...	...	...
61	53421.4(7)	2.44(8)	0.25(8)	53484.2(6)	...	...	...	...	...
62	53485.8(12)	2.37(10)	0.30(7)	53547.4(13)	12.4(4)	2.0(5)	...	...	...
63	53544.8(13)	2.18(7)	0.17(11)	53609.8(6)	9.9(7)	0.5(3)	...	...	...
64	53612.1(6)	2.40(6)	-0.02(13)	53666.7(8)	10.0(2)	0.8(6)	...	...	...
65	53666.5(7)	2.35(5)	0.19(10)	53722.2(5)	11.3(3)	0.3(4)	...	...	...
66	53721.3(5)	3.02(9)	0.29(10)	53775.6(8)	15.0(5)	0.3(8)	...	...	...
67	53776.6(7)	2.14(7)	0.15(8)	53829.3(6)	11.4(4)	1.6(6)	...	...	...
68	53831.3(9)	2.00(8)	0.20(7)	53878.4(7)	9.8(4)	1.0(9)	...	...	...
69	53879.5(8)	2.11(6)	0.53(12)	53925.5(4)	14.1(3)	5.2(3)	...	...	...
70	53924.7(10)	2.05(7)	0.39(18)	53969.4(3)	12.6(2)	2.4(3)	...	...	...
71	53971.4(7)	2.21(7)	0.13(12)	54016.5(7)	12.2(2)	0.6(2)	...	...	...
72	54012.9(9)	1.98(6)	0.27(9)	54058.4(9)	11.0(2)	2.7(2)	...	...	...
73	54057.2(8)	2.05(8)	0.15(9)	54101.1(6)	11.1(3)	1.7(3)	...	...	...
74	54101.7(6)	1.95(8)	0.10(11)	54150.8(6)	11.2(2)	0.9(4)	...	...	...
75	54153.1(6)	2.34(10)	0.30(9)	54203.0(6)	13.2(3)	2.2(8)	...	...	...
76	54202.4(11)	2.02(10)	0.03(9)	54258.8(6)	11.0(3)	0.3(3)	...	...	...
77	54258.2(9)	2.40(7)	0.12(10)	54317.4(7)	12.6(4)	0.8(3)	...	...	...
78	54314.4(9)	2.50(6)	-0.00(9)	54373.5(7)	11.3(3)	1.2(3)	...	...	...
79	54372.3(5)	2.88(6)	0.10(7)	54436.2(8)	14.5(2)	0.9(3)	...	...	...
80	54435.1(6)	1.96(6)	0.21(9)	54494.1(6)	11.2(3)	0.1(6)	...	...	...
81	54495.2(6)	2.50(11)	0.08(8)	54545.2(6)	13.4(5)	-0.2(5)	...	...	...
82	54547.5(8)	1.86(10)	0.17(8)	54596.7(4)	11.5(2)	0.1(2)	...	...	...
83	54597.9(5)	2.60(8)	0.15(7)	54652.0(6)	13.3(3)	0.8(4)	...	...	...
84	54653.7(6)	2.47(9)	0.17(8)	54711.7(6)	9.9(2)	1.1(4)	...	...	...
85	54711.2(7)	2.15(7)	0.11(10)	54767.9(5)	11.1(2)	1.4(2)	...	...	...
86	54767.5(7)	2.01(7)	-0.01(7)	54815.7(5)	10.4(2)	0.3(6)	...	...	...
87	54815.0(5)	2.07(7)	0.19(10)	54868.6(6)	12.0(3)	0.3(4)	...	...	...
88	54871.1(8)	2.43(8)	-0.02(10)	54932.4(7)	12.4(2)	0.3(3)	...	...	...

Table 6 continued

**Table 6** (*continued*)

Cycle	<i>RXTE</i> ASM			<i>Swift</i> BAT			MAXI GSC		
	$T_{\min}^a$	High <sup>b</sup>	Low <sup>c</sup>	$T_{\min}^a$	High <sup>b</sup>	Low <sup>c</sup>	$T_{\min}^a$	High <sup>b</sup>	Low <sup>c</sup>
89	54929.2(7)	2.28(6)	-0.07(11)	54995.1(6)	12.8(3)	0.4(4)	...	...	...
90	54996.7(9)	2.66(8)	0.07(8)	55055.9(6)	10.8(3)	0.8(4)	...	...	...
91	55057.2(6)	2.36(8)	0.06(9)	55112.1(6)	11.1(3)	1.0(2)	55112.8(5)	...	...
92	55113.7(12)	1.89(7)	0.11(7)	55168.6(5)	11.6(2)	0.7(3)	55169.3(4)	0.151(2)	0.016(3)
93	55169.6(5)	2.70(9)	0.23(13)	55224.5(7)	12.1(2)	1.6(5)	55225.1(5)	0.157(3)	0.005(2)
94	55225.2(7)	2.44(9)	0.44(21)	55282.2(6)	14.3(3)	0.3(3)	55281.8(6)	0.141(3)	0.010(3)
95	55282.0(16)	2.40(12)	0.18(12)	55334.7(7)	11.1(4)	1.1(4)	55334.6(4)	0.158(3)	0.006(3)
96	55335.3(7)	2.31(9)	0.33(12)	55388.0(6)	11.7(2)	0.7(4)	55388.1(5)	0.156(3)	0.008(3)
97	55386.8(8)	...	...	55448.7(6)	11.4(4)	0.9(4)	55449.5(8)	0.143(3)	0.007(3)
98	...	...	...	55507.8(5)	11.0(2)	0.8(2)	55507.4(3)	0.136(2)	0.004(3)
99	...	...	...	55567.6(9)	11.2(3)	0.4(4)	55568.0(5)	0.163(3)	-0.001(3)
100	...	...	...	55627.9(7)	11.1(4)	0.1(6)	55628.1(6)	0.182(3)	0.014(4)
101	...	...	...	55684.1(5)	12.8(3)	0.7(4)	55683.7(4)	0.148(3)	0.006(3)
102	...	...	...	55732.6(5)	12.0(4)	0.7(4)	55733.9(5)	0.168(3)	0.010(3)
103	...	...	...	55788.4(4)	13.9(4)	-0.0(3)	55788.6(5)	0.166(3)	0.000(3)
104	...	...	...	55841.7(4)	11.7(2)	1.2(3)	55843.6(4)	0.167(3)	0.013(4)
105	...	...	...	55896.4(3)	13.3(2)	2.1(3)	55896.2(4)	0.147(3)	0.003(3)
106	...	...	...	55950.9(8)	11.2(2)	1.2(4)	55950.5(2)	0.131(3)	0.022(3)
107	...	...	...	55998.6(6)	8.7(3)	2.2(4)	55997.9(5)	0.155(3)	0.007(6)
108	...	...	...	56049.1(5)	12.5(4)	1.2(3)	56048.7(5)	0.169(4)	0.003(4)
109	...	...	...	56105.2(5)	12.9(4)	0.1(4)	56105.0(6)	0.184(4)	0.008(4)
110	...	...	...	56164.7(6)	12.9(3)	1.4(3)	56164.6(7)	0.166(5)	0.001(5)
111	...	...	...	56224.2(6)	12.0(2)	-0.2(3)	56224.5(5)	0.158(4)	-0.001(4)
112	...	...	...	56281.6(5)	12.4(2)	0.6(3)	56281.6(4)	0.166(4)	0.010(5)
113	...	...	...	56338.5(5)	10.9(2)	0.6(6)	56339.3(6)	0.162(4)	0.012(5)
114	...	...	...	56395.2(5)	11.2(2)	0.7(4)	56394.7(7)	0.154(4)	0.002(4)
115	...	...	...	56455.1(6)	11.0(4)	1.0(4)	56454.7(6)	0.162(5)	0.008(5)
116	...	...	...	56515.6(5)	11.0(3)	0.5(4)	56513.1(5)	0.165(4)	0.002(5)
117	...	...	...	56570.7(5)	13.1(3)	1.5(3)	56571.7(5)	0.160(4)	0.021(7)
118	...	...	...	56622.8(4)	11.8(2)	1.4(2)	56623.3(6)	0.188(5)	-0.005(4)
119	...	...	...	56673.3(4)	11.4(2)	-0.3(3)	56673.2(5)	0.171(5)	0.007(5)
120	...	...	...	56730.6(4)	13.3(3)	1.8(3)	56731.4(4)	0.168(5)	0.009(5)
121	...	...	...	56784.4(3)	13.1(3)	0.1(4)	56784.6(4)	0.156(4)	0.021(6)
122	...	...	...	56838.8(6)	11.5(4)	0.4(4)	56838.3(5)	0.178(5)	0.007(5)
123	...	...	...	56892.7(5)	12.5(3)	0.8(3)	56892.8(5)	0.148(6)	0.006(5)
124	...	...	...	56938.2(5)	11.4(3)	2.2(3)	56936.8(6)	0.151(4)	0.021(6)
125	...	...	...	56985.3(9)	11.6(3)	1.8(4)	56983.6(4)	0.136(5)	0.043(6)

*Table 6 continued*



Table 6 (continued)

Cycle	RXTE ASM			Swift BAT			MAXI GSC		
	$T_{\min}^a$	High <sup>b</sup>	Low <sup>c</sup>	$T_{\min}^a$	High <sup>b</sup>	Low <sup>c</sup>	$T_{\min}^a$	High <sup>b</sup>	Low <sup>c</sup>
126	...	...	...	57027.5(11)	11.3(3)	3.5(5)	57028.5(10)	0.135(6)	0.081(8)
127	...	...	...	57061.9(21)	11.4(3)	7.2(3)	57062.9(20)	0.170(5)	0.024(5)
128	...	...	...	57105.3(7)	13.6(3)	4.3(4)	57105.1(8)	0.149(5)	0.013(5)
129	...	...	...	57152.8(5)	12.9(2)	0.4(5)	57153.4(4)	0.171(4)	0.005(6)
130	...	...	...	57207.0(5)	14.3(4)	1.2(5)	57207.1(6)	0.155(4)	0.024(5)
131	...	...	...	57251.5(9)	11.1(4)	2.6(5)	57250.0(6)	0.146(5)	0.024(6)
132	...	...	...	57295.1(6)	11.8(4)	0.2(3)	57294.9(5)	0.165(5)	0.033(7)
133	...	...	...	57342.8(5)	11.3(3)	0.7(3)	57343.9(5)	0.142(4)	-0.000(5)
134	...	...	...	57392.7(4)	11.6(2)	0.3(4)	57392.2(5)	0.182(5)	-0.002(5)
135	...	...	...	57444.8(5)	12.6(4)	0.8(3)	57445.5(2)	0.161(4)	0.018(6)
136	...	...	...	57499.7(4)	12.4(2)	0.9(3)	57499.3(5)	0.163(4)	0.015(5)
137	...	...	...	57556.4(4)	12.3(3)	0.2(3)	57556.9(6)	0.180(5)	-0.008(5)
138	...	...	...	57610.2(5)	12.8(3)	0.4(3)	57608.8(5)	0.227(6)	0.043(5)
139	...	...	...	57661.0(5)	11.4(3)	1.4(3)	57658.9(6)	0.151(4)	-0.005(6)
140	...	...	...	57713.1(7)	11.6(3)	0.9(3)	57713.5(5)	0.167(4)	0.011(5)
141	...	...	...	57769.9(5)	12.6(3)	2.0(3)	57771.9(7)	0.163(5)	0.010(5)
142	...	...	...	57823.1(5)	11.5(3)	0.2(3)	57823.8(5)	0.180(5)	0.001(5)
143	...	...	...	57877.9(5)	13.8(3)	1.1(3)	57879.0(5)	0.137(4)	0.015(5)
144	...	...	...	57930.9(5)	12.5(3)	0.5(6)	57930.3(4)	0.180(4)	0.005(5)
145	...	...	...	57991.1(7)	13.0(3)	1.4(4)	57990.9(5)	0.167(4)	0.002(4)
146	...	...	...	58050.2(10)	12.0(3)	1.8(5)	58049.0(5)	0.160(5)	0.023(5)
147	...	...	...	58103.3(7)	11.7(3)	2.0(7)	58103.2(5)	0.139(4)	0.021(6)
148	...	...	...	58147.5(6)	11.6(4)	1.9(5)	58147.4(5)	0.170(5)	0.016(4)
149	...	...	...	58198.1(5)	12.4(3)	1.2(3)	58197.1(5)	0.163(5)	0.007(5)
150	...	...	...	58251.0(8)	11.6(2)	1.4(4)	58250.6(5)	0.153(4)	0.013(6)
151	...	...	...	58306.4(7)	10.5(4)	3.3(4)	58306.2(6)	0.147(4)	0.006(7)
152	...	...	...	58356.3(5)	11.5(3)	1.7(4)	58356.5(4)	0.161(6)	0.010(6)
153	...	...	...	58404.6(4)	12.4(4)	1.7(6)	58405.0(7)	0.153(6)	0.012(6)
154	...	...	...	58448.5(8)	13.6(3)	2.7(6)	58447.3(5)	0.143(4)	0.016(5)
155	...	...	...	58497.6(6)	...	...	58495.9(5)	...	...

<sup>a</sup>Arrival time (MJD) of superorbital minimum.

<sup>b</sup>High-state count rate. The unit of ASM data is counts s<sup>-1</sup>, while the units of BAT and GSC data are 10<sup>-3</sup> counts cm<sup>-2</sup> s<sup>-1</sup> and counts cm<sup>-2</sup> s<sup>-1</sup>, respectively.

<sup>c</sup>Low-state count rate. The unit is the same as that of the high-state count rate.

B. SPIN PERIOD MEASUREMENTS OF SMC X-1  
WITH MAXI

We list the spin period, spin-down rate,  $T_0$ ,  $T_{\pi/2}$ , number of event collected with MAXI, and the corresponding  $Z_2^2$  value of each superorbitl cycle in Table 7.

**Table 7.** Spin Period Measurements of SMC X-1 with MAXI

Cycle	$T_0^a$ (MJD)	$T_{\pi/2}$ (MJD)	$\nu$ (Hz)	$\dot{\nu}$ ( $10^{-11} \text{ s}^{-2}$ )	Events <sup>b</sup>	$Z_2^2$
91	55141	55142.9052(2)	1.4240083(1)	2.081(4)	9445	181.8
92	55198	55197.3912(2)	1.4241239(1)	2.429(4)	15692	267.1
93	55255	55255.7684(2)	1.4242590(1)	2.382(4)	16150	161.7
94	55310	55310.2545(2)	1.4243534(1)	2.317(5)	14334	170.2
95	55363	55364.7404(2)	1.4244604(1)	2.517(5)	10876	244.2
96	55421	55419.2258(2)	1.4245835(1)	2.097(3)	14014	168.4
97	55481	55481.4955(2)	1.4246899(1)	2.013(4)	14340	119.0
98	55540	55539.8730(2)	1.4248189(1)	2.424(4)	16324	158.2
99	55599	55598.2505(2)	1.4249414(1)	2.403(4)	18080	258.3
100	55656	55656.6278(2)	1.4250781(1)	2.964(4)	17376	182.4
101	55710	55711.1135(2)	1.4251947(1)	2.761(5)	7495	113.3
102	55764	55765.5993(2)	1.4253197(1)	2.800(4)	12980	91.1
103	55818	55816.1927(2)	1.4254376(1)	2.509(5)	17546	379.0
104	55871	55870.6783(2)	1.4255514(1)	2.674(5)	13521	188.2
105	55925	55925.1638(2)	1.4256705(1)	2.360(5)	12391	194.4
106	55976	55975.7574(2)	1.4257661(1)	2.255(6)	9755	142.4
107	56025	56026.3510(2)	1.4258712(1)	2.714(5)	12330	173.2
108	56078	56076.9444(2)	1.4259987(1)	3.106(4)	7902	74.0
109	56137	56135.3218(2)	1.4261344(1)	2.796(3)	7544	89.0
110	56197	56197.5908(2)	1.4262785(1)	2.526(4)	7573	68.0
111	56254	56252.0760(2)	1.4263921(1)	2.700(4)	7877	103.4
112	56311	56310.4530(2)	1.4265115(1)	2.655(4)	10384	98.4
113	56368	56368.8305(2)	1.4266273(1)	2.563(4)	6814	52.8
114	56426	56427.2063(2)	1.4267431(1)	2.457(4)	6643	51.3
115	56485	56485.5846(2)	1.4268652(1)	2.074(4)	6377	47.5
116	56544	56543.9609(2)	1.4269959(1)	2.965(4)	8626	86.5
117	56599	56598.4462(2)	1.4271148(1)	2.335(5)	7963	70.3
118	56649	56649.0391(2)	1.4272283(1)	2.435(5)	6212	87.0
119	56704	56703.5249(2)	1.4273560(1)	3.015(4)	7202	77.2
120	56759	56758.0099(2)	1.4274809(1)	2.605(5)	8359	137.1

*Table 7 continued*

**Table 7** (*continued*)

Cycle	$T_0^a$	$T_{\pi/2}$	$\nu$	$\dot{\nu}$	Events <sup>b</sup>	$Z_2^2$
	(MJD)	(MJD)	(Hz)	( $10^{-11} \text{ s}^{-2}$ )		
121	56812	56812.4948(2)	1.4275901(1)	2.458(4)	8321	101.8
122	56866	56866.9796(2)	1.4276921(1)	2.229(5)	6260	58.3
123	56915	56913.6804(2)	1.4277966(1)	2.030(6)	5258	46.2
124	56961	56960.3825(2)	1.4278905(1)	2.476(6)	7269	67.4
125	57006	57007.0841(2)	1.4279816(1)	2.266(7)	5139	82.3
126	57046	57046.0017(2)	1.4280613(2)	2.494(10)	4491	82.8
127	57085	57084.9198(2)	1.4281527(1)	2.895(8)	5094	72.1
128	57129	57127.7290(2)	1.4282565(1)	2.392(6)	6905	67.4
129	57180	57178.3222(2)	1.4283766(1)	2.982(4)	9046	124.1
130	57229	57228.9153(2)	1.4284871(1)	2.399(8)	4918	57.7
131	57272	57271.7246(2)	1.4285729(1)	2.185(7)	5432	68.5
132	57319	57318.4255(2)	1.4286749(1)	2.523(5)	7664	38.9
133	57369	57369.0190(2)	1.4287774(1)	2.133(5)	5603	100.6
134	57421	57419.6121(2)	1.4288891(1)	2.783(5)	6790	70.6
135	57474	57474.0969(2)	1.4290248(1)	2.804(5)	9057	71.4
136	57528	57528.5814(2)	1.4291431(1)	2.556(4)	8719	80.9
137	57583	57583.0651(2)	1.4292693(1)	2.585(5)	5903	68.2
138	57635	57633.6579(2)	1.4293987(1)	2.426(5)	6992	37.5
139	57687	57688.1433(2)	1.4295118(1)	2.318(5)	9286	113.9
140	57743	57742.6278(2)	1.4296318(1)	2.561(4)	9221	82.8
141	57798	57797.1122(2)	1.4297494(1)	2.400(5)	6332	91.1
142	57852	57851.5973(2)	1.4298754(1)	3.038(4)	7903	74.1
143	57905	57906.0815(2)	1.4299971(1)	2.180(5)	9246	68.5
144	57962	57960.5659(2)	1.4301205(1)	2.325(3)	11013	130.4
145	58022	58022.8334(2)	1.4302410(1)	2.246(4)	6923	59.6
146	58077	58077.3182(2)	1.4303309(1)	1.780(5)	6978	54.4
147	58126	58127.9111(2)	1.4304460(1)	2.507(7)	10793	69.1
148	58174	58174.6116(2)	1.4305565(1)	2.843(5)	8053	69.7
149	58226	58225.2045(2)	1.4306662(1)	2.656(5)	6697	51.2
150	58280	58279.6882(2)	1.4307847(1)	2.605(4)	10275	79.0
151	58333	58334.1727(2)	1.4308939(1)	2.589(5)	10197	136.6
152	58382	58380.8733(2)	1.4310074(1)	2.778(6)	5782	55.1
153	58427	58427.5741(2)	1.4311120(1)	2.663(8)	7757	75.7
154	58473	58474.2743(2)	1.4312158(1)	2.834(5)	9173	77.7
155	58526	58524.8672(2)	1.4313410(1)	2.970(4)	6447	132.1

*Table 7 continued*

**Table 7** (*continued*)

Cycle	$T_0^a$	$T_{\pi/2}$	$\nu$	$\dot{\nu}$	Events <sup>b</sup>	$Z_2^2$
	(MJD)	(MJD)	(Hz)	( $10^{-11} \text{ s}^{-2}$ )		

<sup>a</sup>Epoch zero of the spin frequency measurement. We set it to the midpoint of the segment.

<sup>b</sup>Number of events in the energy range of 2–20 keV. The events collected during  $0.12 < \phi_{\text{orb}} < 0.88$  and  $0.1 < \phi_{\text{sup}} < 0.6$  are used in the analysis.

NOTE—This table is available online at <http://maxi.riken.jp/pulsar/smcx1/>

## REFERENCES

- Barthelmy, S. D., Barbier, L. M., Cummings, J. R., et al. 2005, *SSRv*, 120, 143
- Bildsten, L., Chakrabarty, D., Chiu, J., et al. 1997, *ApJS*, 113, 367
- Buccheri, R., Bennett, K., Bignami, G. F., et al. 1983, *A&A*, 128, 245
- Charles, P., Clarkson, W., Cornelisse, R., & Shih, C. 2008, *New Astronomy Reviews*, 51, 768
- Clarkson, W. I., Charles, P. A., Coe, M. J., et al. 2003, *MNRAS*, 339, 447
- Cleveland, W. S. 1979, *Journal of the American Statistical Association*, 74, 829.
- Cleveland, W. S., & Devlin, S. J. 1988, *Journal of the American Statistical Association*, 83, 596.
- Coe, M. J., Angus, R., Orosz, J. A., & Udalski, A. 2013, *MNRAS*, 433, 746
- Coe, M. J., Burnell, S. J. B., Engel, A. R., Evans, A. J., & Quenby, J. J. 1981, *MNRAS*, 197, 247
- Corbet, R. H. D. 1986, *MNRAS*, 220, 1047
- Corbet, R. H. D., & Krimm, H. A. 2013, *ApJ*, 778, 45
- Dage, K. C., Clarkson, W. I., Charles, P. A., Laycock, S. G. T., & Shih, I.-C. 2019, *MNRAS*, 482, 337
- Deeter, J., Crosa, L., Gerend, D., & Boynton, P. E. 1976, *ApJ*, 206, 861
- Efron, B. 1979, *The Annals of Statistics*, 7, 1.
- Falanga, M., Bozzo, E., Lutovinov, A., et al. 2015, *A&A*, 577, A130
- Foster, G. 1996, *AJ*, 112, 1709
- Foulkes, S. B., Haswell, C. A., & Murray, J. R. 2010, *MNRAS*, 401, 1275
- Fruscione, A., McDowell, J. C., Allen, G. E., et al. 2006, *Proc. SPIE*, 6270, 62701V
- Gerend, D., & Boynton, P. E. 1976, *ApJ*, 209, 562
- Ghosh, P., & Lamb, F. K. 1979, *ApJ*, 234, 296
- Grossmann, A., & Morlet, J. 1984, *SIAM Journal on Mathematical Analysis*, 15, 723.
- Gruber, D. E., & Rothschild, R. E. 1984, *ApJ*, 283, 546
- Henry, P., & Schreier, E. 1977, *ApJL*, 212, L13
- Hickox, R. C., & Vrtilek, S. D. 2005, *ApJ*, 633, 1064
- Holland, P. W., & Welsch, R. E. 1977, *Communications in Statistics - Theory and Methods*, 6, 813.
- Howarth, I. D. 1982, *MNRAS*, 198, 289
- Hu, C.-P., Chou, Y., Ng, C.-Y., Lin, L. C.-C., & Yen, D. C.-C. 2017, *ApJ*, 844, 16
- Hu, C.-P., Chou, Y., Wu, M.-C., Yang, T.-C., & Su, Y.-H. 2011, *ApJ*, 740, 67
- Hu, C.-P., Chou, Y., Yang, T.-C., & Su, Y.-H. 2013, *ApJ*, 773, 58
- . 2014, *ApJ*, 788, 31
- Huang, N. E., Shen, Z., Long, S. R., et al. 1998, *Royal Society of London Proceedings Series A*, 454, 903
- Huber, P. J. 1981, *Robust statistics*, 1981, *Wiley Series in Probability and Mathematical Statistics*, New York: Wiley
- İnam, S. c., Baykal, A., & Beklen, E. 2010, *MNRAS*, 403, 378
- Inoue, H. 2012, *PASJ*, 64, 40
- . 2019, *PASJ*, 71, 36
- Jenke, P. A., Finger, M. H., Wilson-Hodge, C. A., & Camero-Arranz, A. 2012, *ApJ*, 759, 124
- Jurua, E., Charles, P. A., Still, M., & Meintjes, P. J. 2011, *MNRAS*, 418, 437
- Kochanek, C. S., Shappee, B. J., Stanek, K. Z., et al. 2017, *PASP*, 129, 104502
- Krimm, H. A., Holland, S. T., Corbet, R. H. D., et al. 2013, *ApJS*, 209, 14
- Leahy, D. A., & Igna, C. D. 2010, *ApJ*, 713, 318
- Levine, A., Rappaport, S., Deeter, J. E., Boynton, P. E., & Nagase, F. 1993, *ApJ*, 410, 328
- Levine, A. M., Bradt, H., Cui, W., et al. 1996, *ApJL*, 469, L33

- Levine, A. M., Bradt, H. V., Chakrabarty, D., Corbet, R. H. D., & Harris, R. J. 2011, *ApJS*, 196, 6
- Li, X.-D., & van den Heuvel, E. P. J. 1997, *A&A*, 321, L25
- Lucke, R., Yentis, D., Friedman, H., Fritz, G., & Shulman, S. 1976, *ApJL*, 206, L25
- Matsuoka, M., Kawasaki, K., Ueno, S., et al. 2009, *PASJ*, 61, 999
- Mihara, T., Nakajima, M., Sugizaki, M., et al. 2011, *PASJ*, 63, S623
- Neilsen, J., Hickox, R. C., & Vrtilek, S. D. 2004, *ApJL*, 616, L135
- Nelder, J. A., & Mead, R. 1965, *The Computer Journal*, 7, 308.
- Ogilvie, G. I., & Dubus, G. 2001, *MNRAS*, 320, 485
- Parmar, A. N., Oosterbroek, T., dal Fiume, D., et al. 1999, *A&A*, 350, L5
- Petterson, J. A. 1977, *ApJ*, 218, 783
- Pike, S. N., Harrison, F. A., Bachetti, M., et al. 2019, *ApJ*, 875, 144
- Price, R. E., Groves, D. J., Rodrigues, R. M., et al. 1971, *ApJL*, 168, L7
- Pringle, J. E. 1996, *MNRAS*, 281, 357
- . 1997, *MNRAS*, 292, 136
- Pringle, J. E., & Rees, M. J. 1972, *A&A*, 21, 1
- Raichur, H., & Paul, B. 2010, *MNRAS*, 401, 1532
- Rawls, M. L., Orosz, J. A., McClintock, J. E., et al. 2011, *ApJ*, 730, 25
- Reynolds, A. P., Hilditch, R. W., Bell, S. A., & Hill, G. 1993, *MNRAS*, 261, 337
- Schreier, E., Giacconi, R., Gursky, H., Kellogg, E., & Tananbaum, H. 1972, *ApJL*, 178, L71
- Scott, D. M., Leahy, D. A., & Wilson, R. B. 2000, *ApJ*, 539, 392
- Shappee, B. J., Prieto, J. L., Grupe, D., et al. 2014, *ApJ*, 788, 48
- Staubert, R., Klochkov, D., Postnov, K., et al. 2009, *A&A*, 494, 1025
- Staubert, R., Klochkov, D., Vasco, D., et al. 2013, *A&A*, 550, A110
- Still, M., & Boyd, P. 2004, *ApJL*, 606, L135
- Sugizaki, M., Mihara, T., Serino, M., et al. 2011, *PASJ*, 63, S635
- Takagi, T., Mihara, T., Sugizaki, M., Makishima, K., & Morii, M. 2016, *PASJ*, 68, S13
- Trowbridge, S., Nowak, M. A., & Wilms, J. 2007, *ApJ*, 670, 624
- Udalski, A. 2003, *AcA*, 53, 291
- Ulmer, M. P., Baity, W. A., Wheaton, W. A., & Peterson, L. E. 1973, *Nature Physical Science*, 242, 121
- Val Baker, A. K. F., Norton, A. J., & Quaintrell, H. 2005, *A&A*, 441, 685
- van der Meer, A., Kaper, L., van Kerkwijk, M. H., Heemskerk, M. H. M., & van den Heuvel, E. P. J. 2007, *A&A*, 473, 523
- Wang, Y.-H., Yeh, C.-H., Young, H.-W. V., Hu, K., & Lo, M.-T. 2014, *Physica A Statistical Mechanics and its Applications*, 400, 159
- Wijers, R. A. M. J., & Pringle, J. E. 1999, *MNRAS*, 308, 207
- Wojdowski, P., Clark, G. W., Levine, A. M., Woo, J. W., & Zhang, S. N. 1998, *ApJ*, 502, 253
- Wu, Z., & Huang, N. E. 2009, *AADA*, 1, 1.
- Yatabe, F., Makishima, K., Mihara, T., et al. 2018, *PASJ*, 70, 89
- Yeh, J.-R., Shieh, J.-S., & Huang, N. E. 2010, *Advances in Adaptive Data Analysis*, 02, 135.